

available at www.sciencedirect.comjournal homepage: www.elsevier.com/locate/jmbbm

Review article

Biological materials: A materials science approach[☆]

Marc A. Meyers*, Po-Yu Chen, Maria I. Lopez, Yasuaki Seki, Albert Y.M. Lin

University of California, San Diego, La Jolla, CA, United States

ARTICLE INFO

Article history:

Received 25 May 2010

Received in revised form

20 August 2010

Accepted 22 August 2010

ABSTRACT

The approach used by Materials Science and Engineering is revealing new aspects in the structure and properties of biological materials. The integration of advanced characterization, mechanical testing, and modeling methods can rationalize heretofore unexplained aspects of these structures. As an illustration of the power of this methodology, we apply it to biomineralized shells, avian beaks and feathers, and fish scales. We also present a few selected bioinspired applications: Velcro, an Al₂O₃-PMMA composite inspired by the abalone shell, and synthetic attachment devices inspired by gecko.

© 2010 Elsevier Ltd. All rights reserved.

Contents

1. Introduction and basic components	1
2. Hierarchical nature of biological materials	3
3. Structural biological materials	5
3.1. Abalone shell	5
3.2. Toucan and hornbill beaks	14
4. Functional biological materials	17
4.1. The gecko foot	18
4.2. Tree frog	20
4.3. Abalone foot attachment	21
5. Bioinspired materials and structures	23
6. Conclusions	29
Acknowledgements	29
References	29

1. Introduction and basic components

Biological Materials Science is a new and rapidly growing branch of Materials Science and Engineering. It has three

distinct but interrelated components:

- Biological Materials: natural materials
- Biomaterials: synthetic materials in biomedical applications
- Biomimetics: bioinspired materials and design

[☆] Dedicated to the memory of Mia Tegner, who kept the abalone used in our research and died in a tragic diving accident, after spending her career as marine biologist studying abalone, who lives through them.

* Corresponding author. Tel.: +1 858 534 4719; fax: +1 858 534 5698.

E-mail address: mameyers@ucsd.edu (M.A. Meyers).

1751-6161/\$ - see front matter © 2010 Elsevier Ltd. All rights reserved.

doi:10.1016/j.jmbbm.2010.08.005

Table 1 – Principal components of biological materials.

Hard component: minerals	Soft component: organic macromolecules
Calcium carbonate (CaCO ₃)	Collagen (Types I, II, . . . , XXVIII)
Calcium phosphate (hydroxyapatite, Ca ₁₀ (PO ₄) ₆ (OH) ₂)	Keratin
Silica (SiO ₂)	Chitin
Magnetite (Fe ₃ O ₄)	Elastin
Copper oxide	Cellulose
	Resilin and Abductin

There is overlap between these three components. For instance, biological materials have been successfully used in a number of biomedical applications. Examples are biological scaffolds, coral used in bone regeneration, collagen used in implants, etc. (e.g. [Stella et al., 2010](#)).

The prominence of this field can be assessed by the three international conferences on Mechanics and Biomaterials & Tissues (2005, 2007, 2009), organized by the Journal of Mechanical Behavior of Biomedical Materials, by the yearly Biological Materials Science Symposia held at the Annual TMS-AIME meetings (2006–2010), and by the number of sessions and symposia dedicated to this theme at the Materials Research Society meetings.

There have also been a number of overview articles presenting the field in a broad manner. Noteworthy among them are overviews in Progress in Materials Science ([Meyers et al., 2008a](#)) and in JMBBM ([Chen et al., 2008a](#)), and articles dealing with broader aspects of biomineralization ([Lowenstam and Weiner, 1989](#); [Mann et al., 1993](#); [Weiner and Addadi, 1997](#); [Mann, 2001](#); [Ehrlich, 2010](#)) and structural biological materials ([Vincent and Currey, 1980](#); [Vincent, 1991](#); [Mayer, 2005](#); [Meyers et al., 2006](#); [Fratzl and Weinkamer, 2007](#); [Chen et al., 2008b](#); [Buehler et al., 2008](#); [Espinosa et al., 2009](#); [McKittrick et al., 2010](#)). The book *Collagen* edited by [Fratzl \(2008\)](#) presents a comprehensive treatment on the subject. This article will focus primarily on recent research carried out by our group as well as on a few selected biomimetic applications.

It is important to emphasize that some knowledge of biology is also important. Significant misunderstandings can arise if researchers are ignorant of, for example, animal anatomy and physiology, the lifestyle of animals (since their activities determine the applied loadings) and cell biology/biochemistry which determines how structural parts are created and maintained. In an analogy, the same potential errors can arise when materials scientists working on engineering projects proceed without an understanding of the engineering structures in which their materials will be used in.

Biological materials and structures have unique characteristics that distinguish them from synthetic counterparts. These are shown in the schematic ([Arzt, 2006](#)) figure, expanded to a hexahedron. The six components are presented below:

- The structures are assembled from the bottom-up, rather than from the top-down. This is a necessity of the growth process, since there is no availability of an overriding scaffold. This characteristic is called ‘self-assembly’.

- Many components serve more than one purpose; for instance, the skin protects the organism and regulates the temperature; bone is a structural component as well as a factory for red blood cells. Thus, the structures are called ‘multifunctional’.
- The properties are highly dependent on the level of water in the structure. There are some remarkable exceptions, such as enamel, but this rule applies to most biological materials and is of primary importance.
- Evolution, environmental constraints, and the limited availability of materials dictate the morphology and properties. The principal elements available are oxygen, nitrogen, hydrogen, calcium, phosphorous, silicon, and carbon. In addition, trace elements (e.g. Fe) have been found to be crucial for phase determination in some systems, for example, iron oxide in radular teeth of chiton ([Saunders et al., 2009](#); [Weaver et al., 2010](#)). The most useful synthetic metals (iron, aluminum, copper) are virtually absent and are only present in minute quantities and highly specialized applications. The processing of these elements requires high temperature processes not available in natural organisms.
- Except for a few remarkable exceptions, the synthesis of biological materials is conducted in an aqueous environment at ambient temperature and pressure of 1 atm.
- The structures are hierarchical, i.e., they have different scale levels conferring distinct properties.

[Table 1](#) shows the principal components of biological materials. They can be divided into two groups: organic materials and biominerals. Organic materials that can be likened to polymers in MSE, provide, for the most part, a greater ability to undergo deformation, whereas the minerals sustain loading. The organic components can be extended in tension, whereas the ceramic resists primarily compression (e.g., tooth enamel). Few biological systems are subjected to uniaxial tension (exceptions being ligaments and tendons), but flexure is a common mode of loading. In flexure, one half of the cross-section is subjected to compression and the other half to tension. It is only in rare occasions that minerals are not present in combination with organic materials. The organic components, in turn, have a wide variety of structures that confer uniaxial, biaxial, or triaxial properties.

The basic molecular units of the organic components are amino acids organized primarily into polypeptides and polysaccharides. Polysaccharides are the building blocks of cellulose and chitin. Polypeptides form proteins. Proteins are prominent in mammals and comprise most of the extracellular material. The principal protein in mammals is collagen, a fibrillar organic molecule. The basic structure

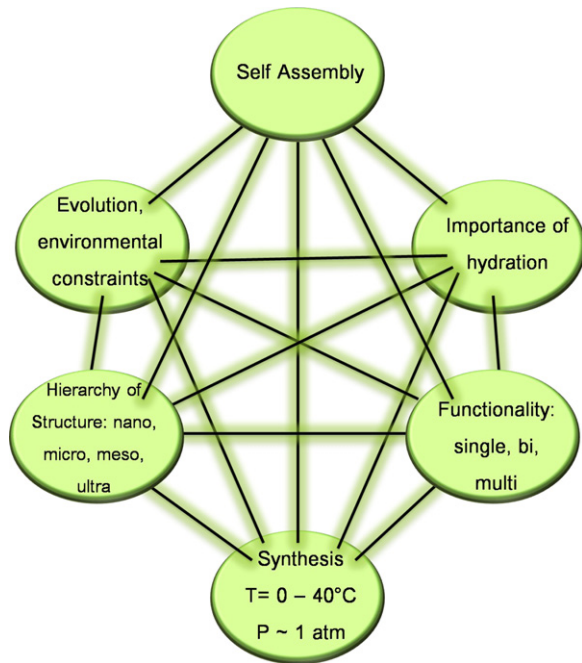


Fig. 1 – Schematic representation of characteristic constraints/components in the study of biological systems. Source: Modified from Arzt (2006).

starts with three polypeptide chains forming a triple helix. These polypeptides contain repeating amino acid motifs (Gly-X-Y) where X and Y can be any amino acid. The chains form right-handed helices and the glycine residues are on the inside of the helix, whereas the X and Y amino acids are exposed, on the outside. The macromolecular units have approximately 300 nm length. Fig. 2(a) shows the polypeptide chains forming tropocollagen and the collagen units bonding in a head-to-tail arrangement, with gaps and overlap regions. The macromolecules are attached to each other and the terminations form gaps that reveal themselves, in transmission electron microscopy, by the characteristic banded pattern with a repeat distance of 64–67 nm. This is the stagger distance between adjacent molecules. Fig. 2(b), (c) show the characteristic pattern revealed in antler collagen. The fibrils have a diameter of 100 nm. They assemble themselves into fibers and other arrays that can be one, two, or tridimensional. Fibrillar collagen (Types I, II, II, V, XI, XXIV, and XXVII) is the most important of the over 20 types of collagen in humans: Type I is the most common, found primarily in skin, tendon, bone, lung, and arteries/veins; Type II, in cartilage; Type III, found in very elastic tissues. Collagen has been called, very appropriately, the ‘steel’ of biological materials by Fung (1993), not because of its properties but because of its multiple and diverse applications.

2. Hierarchical nature of biological materials

This is a unique aspect that defines biological materials, as seen in the hexagon of Fig. 1. One can also think of synthetic materials as hierarchical, but in many cases they only have 2 or 3 levels, whereas biological materials

have 4–8. In synthetic materials the mechanical strength is designed into the structure primarily at the micrometer and millimeter levels. On the other hand, the elastic modulus is the direct result of inter-atomic bonding, which operates at the nanometer level. Hence, the grains in metals and the fiber bundles in composites are the principal hierarchical levels. Biological materials also have an important difference: self-healing capability, enabled by the cells extant in the extracellular material. Thus, the material can recover its original properties. There is a complex interplay that takes place between the different levels of hierarchy that will be analyzed later in this section.

In previous reviews, we have presented the hierarchical structure of abalone (Lin and Meyers, 2005), crab exoskeleton (Chen et al., 2008c), antler (Chen et al., 2009; Launey et al., 2010a), horn (Tombolato et al., 2010), all studied by members of our group. We illustrate this concept here for two additional materials, avian feather and fish scales. Fig. 3(a) shows a schematic of a feather and several SEM micrographs at increasing magnifications. The feather rachis (central shaft) has a cellular core contained in a solid envelope. Both are keratin. The internal foam has a fascinating structure. It consists of cells with approximate diameter of 10 μm , in the case of the *Falco sparverius* primary remiges (flight feathers located on the posterior side of the wing) shown in Fig. 3(a). If one images the cell walls at a higher magnification, one recognizes that they are not solid but are, in turn, composed of fibers with a diameter of ~ 200 nm, as shown in Fig. 3(b). Thus, one has a two-level cellular structure that minimizes, as required, weight. The advantage, in terms of density, of having a two-level hierarchy in the cells, is readily obtained from:

$$\text{For level I, } \frac{\rho_I}{\rho_{II}} = C_1 \left(\frac{t_1}{l_1} \right)^2 \quad (1)$$

$$\text{For level II, } \frac{\rho_{II}}{\rho_s} = C_2 \left(\frac{t_2}{l_2} \right)^2 \quad (2)$$

where ρ_I is the density of the cellular structure at level I, ρ_{II} is the density of the porous strut, and ρ_s is the density of the solid material, respectively. There are two characteristic dimensions: the cell size, l , and the strut thickness, t . C_1 and C_2 are proportionality constants.

$$\text{Thus, } \frac{\rho_I}{\rho_s} = C \left(\frac{t_1 t_2}{l_1 l_2} \right)^2 \quad (3)$$

If the two levels are geometrically similar, $t_1/l_1 \approx t_2/l_2 \approx t/l$, and:

$$\frac{\rho_I}{\rho_s} = C \left(\frac{t}{l} \right)^4 \quad (4)$$

Thus, the relative density ρ_I/ρ_s varies as the fourth order of the geometric ratio t/l . This is indeed a very strong dependence.

Fig. 4 shows the hierarchy of the scales in a large river fish, the *Arapaimas gigas*. This fish can weigh as much as 200 kg. It lives primarily in Amazon basin lakes. It is covered with scales having up to 10 cm length. These scales have a collagen interior with a highly mineralized external layer. The mineral phase is non-stoichiometric hydroxyapatite, the same as that in bones. The collagen

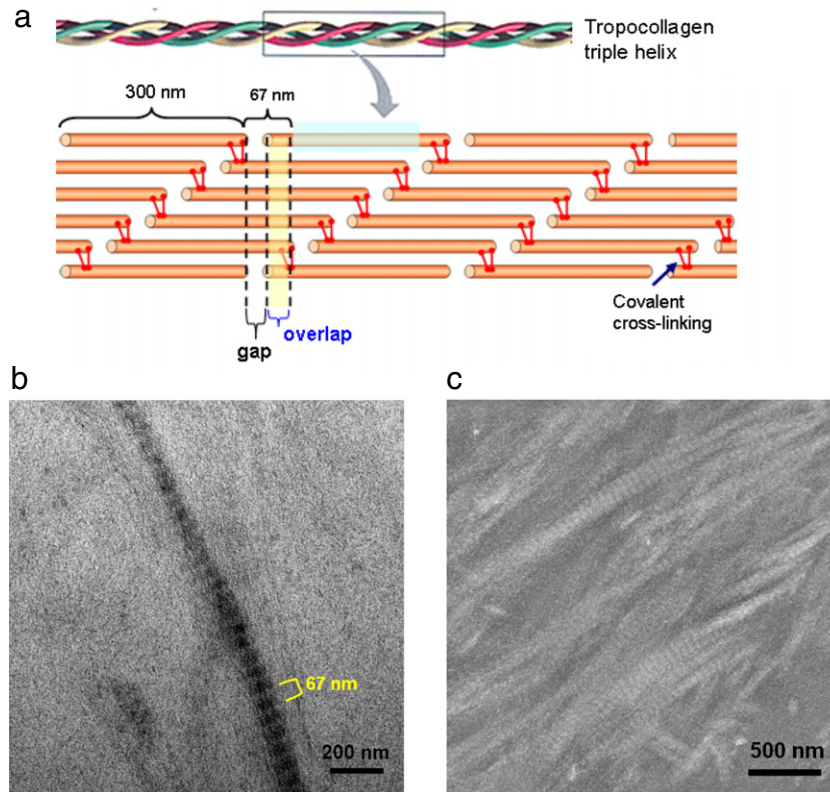


Fig. 2 – (a) Collagen structure, starting with three polypeptide chains forming units ~300 nm long. Overlaps and gaps generate characteristic pattern with 64–67 nm periodicity (b) TEM micrograph of a Type I collagen fibril obtained from demineralized elk antler showing characteristic 67 nm periodicity; (c) Maximum intensity projection (MIP) assembled from series of TEM images showing the structural organization of collagen fibrils.

Source: Courtesy of P.-Y. Chen, unpublished results.

fibers form a cross-lamellar arrangement which produces a laminate composite structure. This structure can undergo significant non-elastic deformation prior to failure, providing considerable toughness. The piranha (*Serrasalminae*) is one of the principal predators in seasonal lakes, in which fish get trapped. Its teeth form triangular arrays creating a guillotine action that is highly effective in slicing through muscle. We performed mechanical tests on the scales and teeth and characterized both (Meyers et al., in preparation). The cutting and puncturing ability of the piranha teeth were evaluated and it was demonstrated that they cannot penetrate the *Arapaimas* scales, which provide protection against them because of the hierarchy of their construction. The ability of the *Arapaimas* to resist the attack of piranha is clearly the result of the hierarchical structure displayed in Fig. 4, consisting of a cross-lamellar arrangement of collagen fibers covered by a highly mineralized external shell.

The recognition that the hierarchy of the structure is an essential feature of biological materials is leading to analyses of a more rigorous nature, beyond the descriptive schematics abundant in the literature. The analytical approach developed by Gao et al. (Gao et al., 2003; Ji and Gao, 2004; Gao, 2006; Yao and Gao, 2008) is noteworthy. Fig. 5(a) shows a self-similar hierarchical structure constructed in a simple and logical manner: the different levels are geometrically similar

and the only difference is the scale. There are two components: the discontinuous ceramic and the continuous collagen phase, in a structure initially proposed by Jäger and Fratzl (2000). However, this “Russian doll” hierarchy is also an approximation, since it assumes that all levels are geometrically similar. In actual structure, each hierarchical level has its own structure, as will become obvious from the discussion below. There is significant evidence in the literature that the strength, as measured by hardness, decreases as one marches up the spatial scale. The converse is true for toughness, as measured by the ability to resist crack propagation. Fig. 5(b) shows these combined effects in a schematic manner. The decrease in strength can be rationalized in a simple manner by the existence of flaws of greater and greater dimensions as the sample size is increased. This is a direct consequence of Weibull statistics. The decrease in hardness is connected to the greater availability (or ease of generation) of defects as the indentation size is increased. In the case of minerals, the strength reaches the theoretical value (equal to approximately 10% of Young’s modulus) when the scale is reduced to the nanometer scale. The increase in toughness with increasing scale is a fascinating effect that counteracts the decrease in strength. A growing crack will encounter both intrinsic and extrinsic (in the terminology of Ritchie’s group (Nalla et al.,

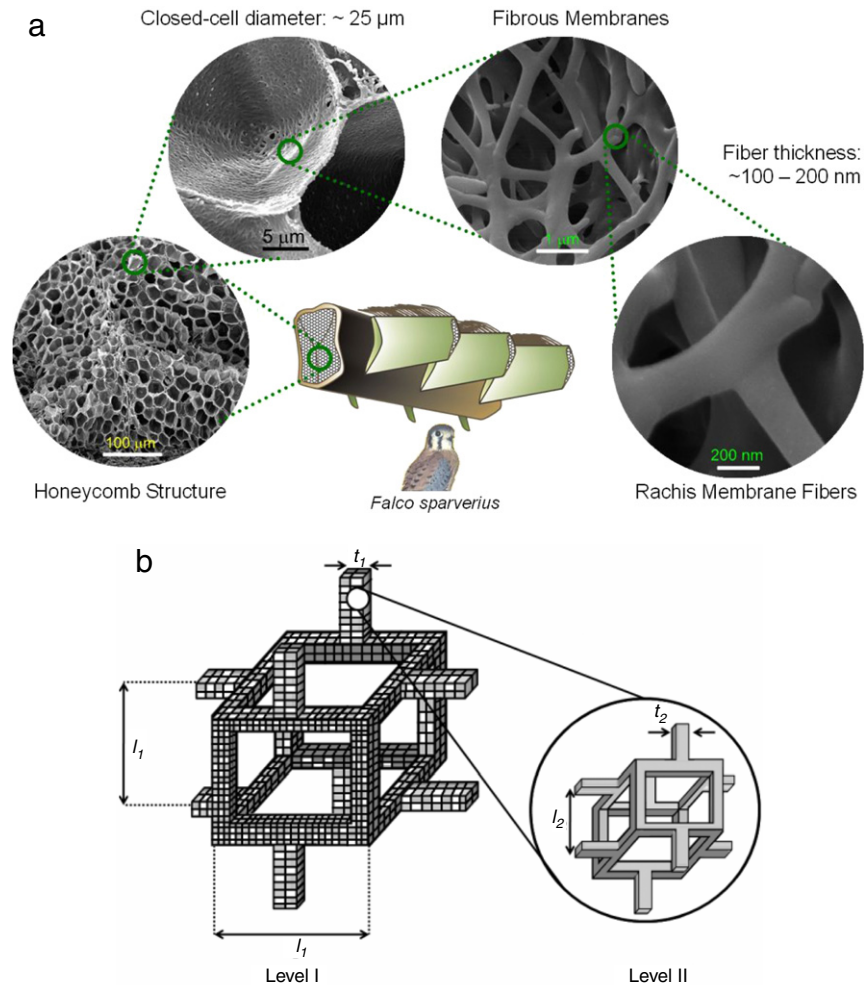


Fig. 3 – (a) Schematic of falcon feather along with scanning electron micrographs; (b) Schematic drawing showing two-level hierarchy of open cell structure in feather.

Source: (a) Courtesy of S.G. Bodde, unpublished research.

2003, 2005; Yang et al., 2006)) barriers as it propagates. The nature and effectiveness of these mechanisms changes with the hierarchical scale and this explains the toughness increase. The hierarchical levels establish a balance between these two mechanical properties.

The hierarchical structure of biological materials needs to be analyzed with a greater emphasis on the mechanisms at the various levels. This is currently only happening in a few materials. The hierarchy of bone was presented by Weiner and Wagner (1998); Rho et al. (1998); Buehler (2007) as composed of seven levels. For the abalone shell, extensively investigated by our group, one can establish five different levels. The self-similar picture of Fig. 5(a) is an oversimplification, and one cannot invoke the same deformation and failure mechanisms at the different levels. Fig. 6 shows the five levels identified for abalone nacre:

- Level I is the molecular structure of the chitin fibers that are the structural components of the intertile organic layers and of the atomic crystalline structure of the aragonite (which might incorporate nanosized islands).

- Level II is composed of the mineral bridges between tiles, with a diameter of 20–60 nm; it also comprises the sandwich structure of the organic intertile layer, with a core consisting of a random dispersion of chitin fibrils and a thickness equal to the length of the mineral bridges (~20 nm).
- Level III are the well recognized hexagonal tiles, with lateral dimensions of 10 μm and thickness of 0.5 μm. These tiles are, in general hexagonal, but not always. They also have a distribution of lateral dimensions.
- Level IV are the mesolayers, which are formed by seasonal fluctuations and are characterized by a thick organic layer (thickness ~200 μm) separating tile assemblages with approximately 0.1–0.3 mm.
- Level V is the entire structure that, because of its architecture (dome shape, thickness distribution, etc.) is optimized for strength and toughness.

These two examples (in Figs. 5 and 6) illustrate what needs to be done for other hierarchical materials: a quantitative hierarchical structure division into levels, followed by the analysis of the deformation and failure mechanisms at the different levels.

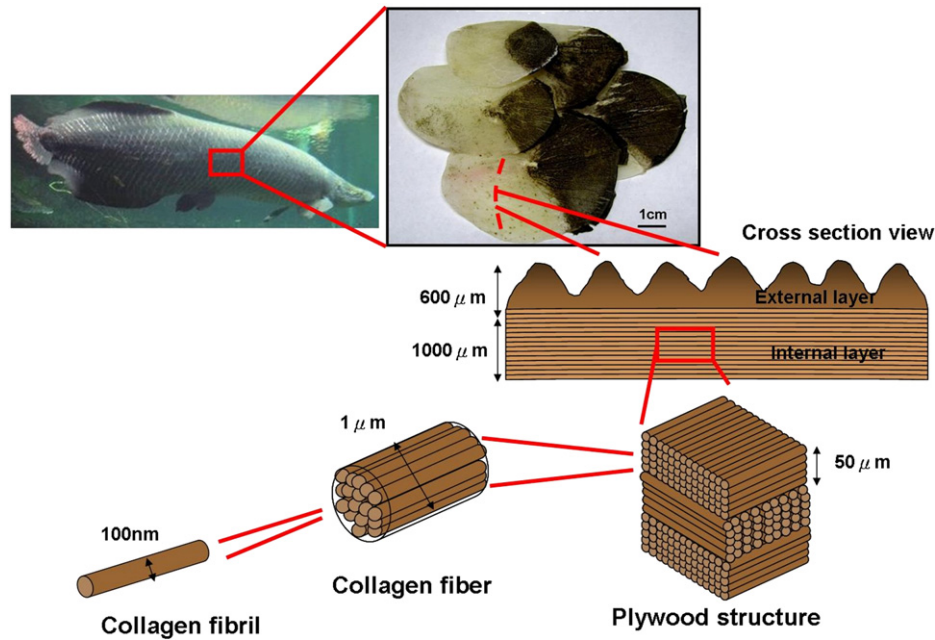


Fig. 4 – Hierarchical structure of the *Arapaimas gigas* scales.
Source: Y.S. Lin et al., unpublished results, 2010.

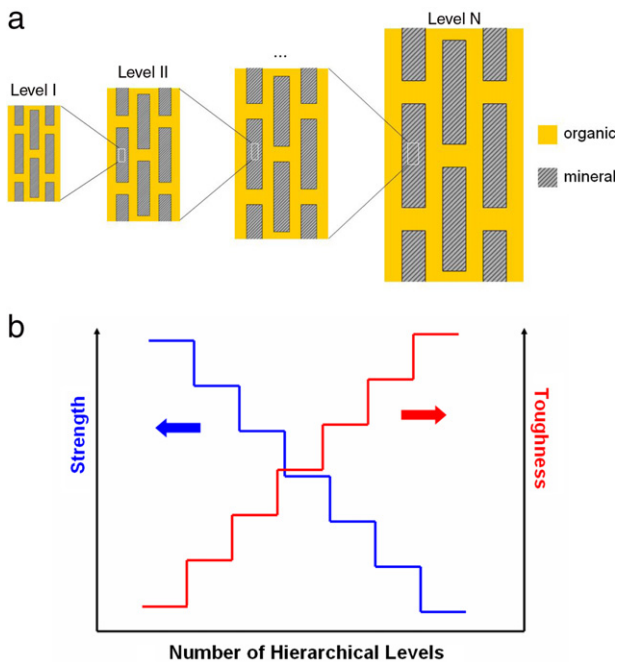


Fig. 5 – Schematic drawings (a) showing self-similar hierarchy (analogous to a Russian doll) with levels I, II, ..., N ; (b) strength and toughness as a function of number of hierarchical levels.

Source: (a) Adapted from Gao (2006).

3. Structural biological materials

We will focus in this section on two biological systems that we have investigated in detail, the abalone shell and the

toucan and hornbill beaks. Our previous overviews in this journal have covered bone, teeth, horn, crab exoskeleton, and antler (Chen et al., 2008a; McKittrick et al., 2010). Table 2 provides an overview of the biological materials under past or current investigation by members of our group.

3.1. Abalone shell

Two aspects of the abalone shell have been investigated: growth and structure/property relations. They are related, i.e., growth determines the structure, which, in its turn, is responsible for its outstanding toughness.

Three techniques were used for extracting specimens for growth observations: the flat pearl, the trepanning techniques described by several groups (Fritz et al., 1994; Belcher et al., 1996; Shen et al., 1997; Meyers et al., 2008b; Lin et al., 2008), and a simpler method, which consists simply of removing a wedge of the shell and observing it (Meyers et al., 2009). The trepanning and flat pearl (glass slide) techniques gave equivalent results, which are shown in the sequence of Fig. 7. The central picture is a cross-section (fracture) of the shell. The growth proceeds from bottom to top. The bottom part is a thick organic mesolayer; it is characteristically smooth. The reinitiation of growth after a prolonged period of rest takes place in stages. First, columnar aragonite crystals are formed with the fast growth direction (c-axis), pointing up. These crystals radiate from the nucleation sites and form a characteristic spherulitic pattern. Eventually, the tile growth pattern replaces it, shown on the top of the central picture. The same sequence occurs when a glass slide is applied to the growing surface of the abalone and removed after predetermined periods of time. Fig. 7(b) shows an array of such slides glued to the growth surface of the shell. They are readily covered by the mantle after the animal is returned to

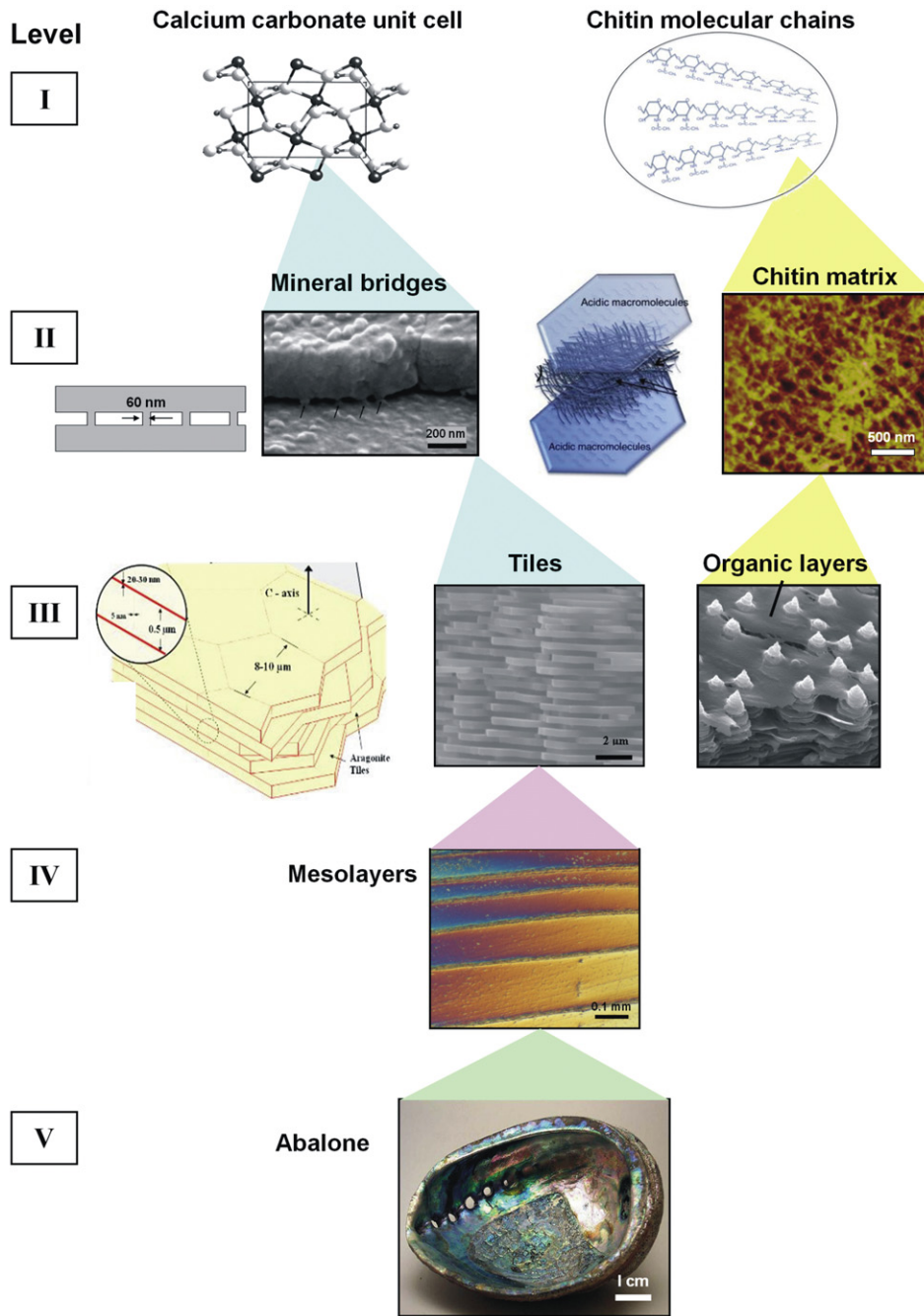


Fig. 6 - Hierarchical structure (5 levels) of the abalone nacre from nano, micro, to meso to structural length scales.

Table 2 - Principal biological materials investigated at UC San Diego in the period 2000-2010.

Mammal	Fish	Bird	Invertebrates
Teeth and Tusks	Scales-Arapaimas	Beaks	Mollusk shells
— hippo	Teeth — piranha	— toucan	— abalone
— warthog	— shark	— hornbill	— conch
Armadillo carapace		Feather	— clam
Antlers and Horns		Claw	Arthropod
		Skin	Exoskeletons
			— crab
			— horseshoe crab
			Sponge spicules

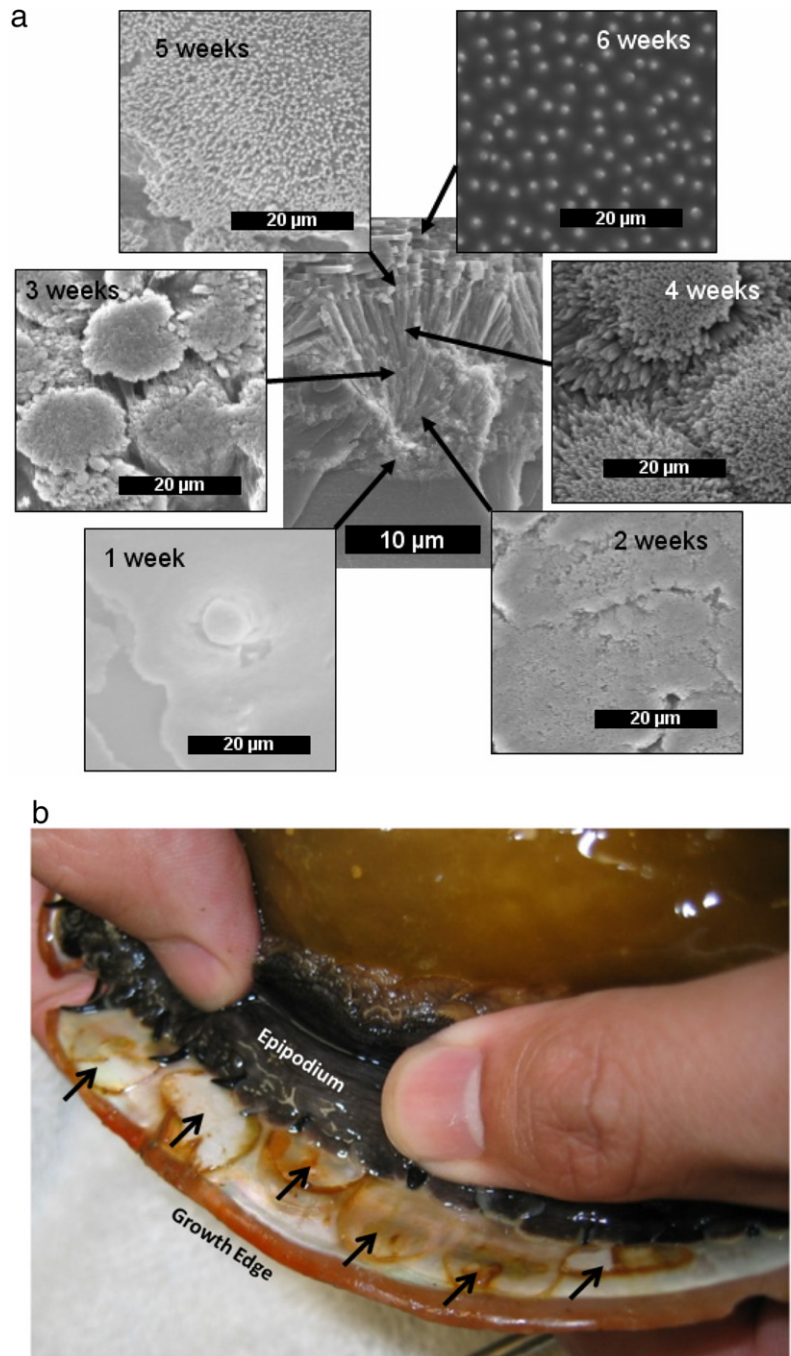


Fig. 7 – (a) Sequential growth of abalone nacre from flat pearl experiment; (b) Glass slides (depicted by arrows) embedded in abalone shell; flat pearl technique.

Source: (a) Adapted from Lin et al., Acta Biomater. (2008); (b) Adapted from Lopez et al., MSEC (in press).

water and mineralization takes place on them. This is shown for intervals varying from 1 to 6 weeks in the peripheral pictures of Fig. 7(a). These pictures represent top views taken from flat pearls. After 3 weeks, the columnar growth is still predominant. However, at six weeks a remarkable change has taken place: growth cones are observed, under an organic layer. More recent experiments indicate that the transition time to tile growth is dependent on the outside conditions. The growth in colder water is sluggish and the transition is slow. Another noticeable effect is the feeding of

the abalone. Fig. 8 shows sequential growth results 1 week after implantation (Lopez et al., in press). Tile growth takes place at 21 °C when abalone was regularly fed (Fig. 8(a)). The formation of tiles is reestablished after 1 week. The growth cones can be seen under the organic layer that completely sagged upon removal of sample from water. In contrast, growth at 15 °C with abalone regularly fed still shows the columnar pattern (Fig. 8(b)); similarly, growth at 20 °C without food available is also columnar (Fig. 8(c)).

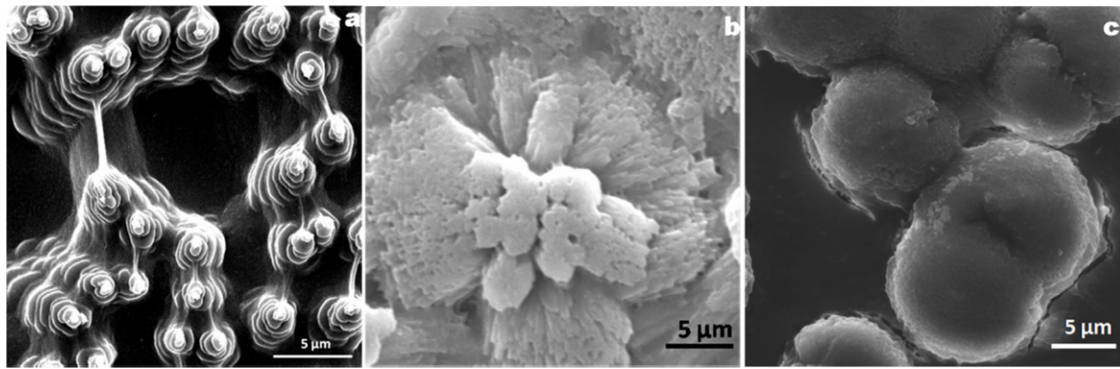


Fig. 8 – Sequential growth result 1 week after implantation. (a) Growth at 21 °C and abalone was regularly fed; (b) Growth at 15 °C with abalone regularly fed; (c) Growth at 20 °C without food available.

Source: Adapted from Lopez et al., MSEC (in press).

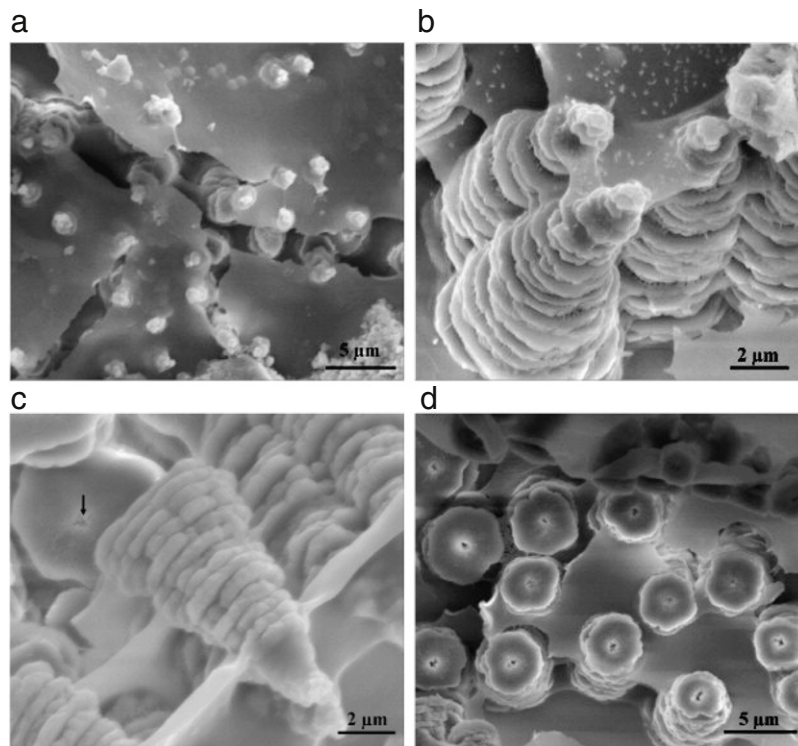


Fig. 9 – Growth surface in red abalone (coated specimen, high vacuum SEM): (a) overall view showing mineral apices and flat organic layer; (b) cracked organic layer; (c) detailed view of three terraced growth sequences; (d) top view of fractured terraced growth sequences exposing incompletely grown tiles with central holes. Arrow in (c) denotes central core orifice revealed by fracture of terraced cone.

Source: Adapted from Meyers et al., MSEC (2009).

The details of this growth pattern are much more clearly seen in Fig. 9. Fig. 9(a) was taken with the environmental mode of the SEM; the top organic layer (“canopy”) is cracked, revealing the growth of the cones (“Christmas tree” pattern) underneath. Using the high vacuum mode leads to drying of the organic layer and shrinkage, resulting in extensive cracking. The mechanical response of this layer is radically altered by the removal of water; it becomes hard and brittle. This was indeed fortuitous and enabled the clear observation of the growth cones, Fig. 9(b). In places, the shrinking of the

organic layer breaks the cones which are seen in Fig. 9(c) (sideways). In Fig. 9(d) the tops of the growth cones were removed and the base tiles are shown. Each one has a hollow core; there is still some disagreement as to the origin and function of the hollow core. Whereas Meyers et al. (2009) hypothesized that this was due to simultaneous growth of three or more new tiles at each layer, leaving a depleted region in the center, Checa et al. (2009) suggest that there is a growing central organic-rich core. In a counterargument,

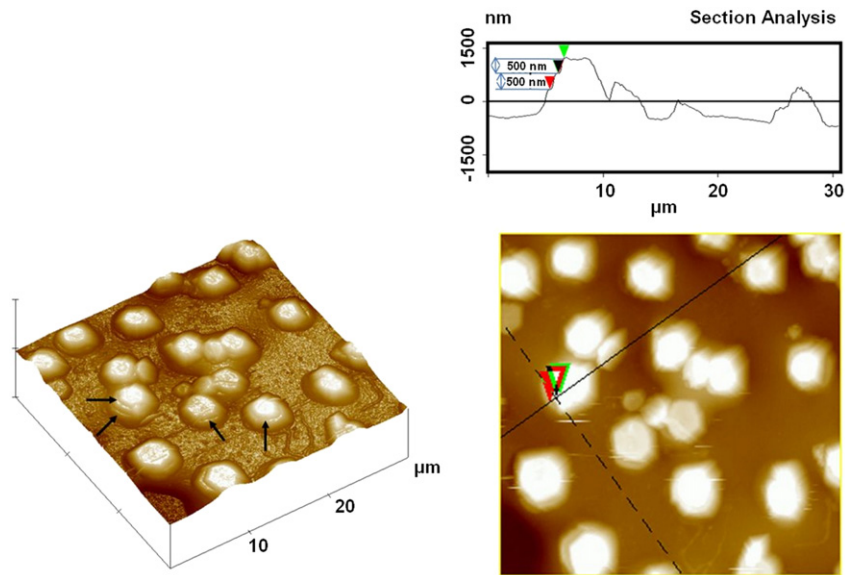


Fig. 10 – Atomic force microscopy of green abalone in tridimensional representation: arrows denote boundary between successive layers in stacks (terraced cones). Section analysis of abalone mineral tiles protruding from surface along line indicated in the micrograph (vertical distances between lines ~500 nm). Source: Adapted from Meyers et al., MSEC (2009).

Meyers et al. (2009) show specimens where this central core is absent.

The same growth surfaces were imaged by AFM and the growth cones are shown as light regions in Fig. 10. A depth trace was made along the line marked on the right-hand side. It shows the characteristic 500 nm steps that correspond to the thickness of the tiles. Arrows show the steps in the perspective view.

The organic layer is imaged by SEM in Fig. 11(a). It has holes that have approximately 20–60 nm in diameter. These holes enable the continuation of growth from one layer to the next and the formation of bridges, which will be discussed below. They also ensure that the same crystallographic orientation is maintained from layer to layer in the same stack. Fig. 11(b) shows the growth mechanism as is thought to occur. The animal periodically creates and deposits the organic layer, whose core is composed of chitin fibers. Growth in the *c*-direction is arrested but eventually restarted once the crystal can penetrate and traverse the holes. The membrane is permeable to Ca^{2+} and CO_3^{2-} ions and lateral growth can therefore take place after a membrane is deposited. Eventually the lateral growth of the tiles is arrested when they impinge upon each other. It is interesting to note that the lateral organic layer between tiles at the same height (arrow B) is less visible than the top ones (arrows A). The SEM inset in Fig. 11(b) shows this through backscattering. This is in perfect agreement with recent results by Checa et al. (2009) and dismisses the idea of a preexisting three-dimensional scaffold as a figment of the imagination. In region B we probably have remains of organics pushed out by the lateral growth fronts. This is analogous to the zone refining process in metallurgy, where the concentration of impurities in the liquid gradually increases as the solidification process advances, expelling the impurities.

By demineralizing the shell using 0.6N HCl, it was possible to image the central core of the organic layer (Fig. 12(a)). It consists of chitin fibrils having a diameter of ~20 nm. They had been previously imaged by AFM and the SEM picture confirms their structure. The chitin network provides the mechanical strength to the organic layer. The chitin core is surrounded by acidic macromolecules that attach themselves to the top and bottom surfaces of the tiles (Fig. 12(b)) (Sarikaya et al., 1990; Checa et al., 2009).

It was possible to establish, in a preliminary and semi-quantitative manner, the mechanical strength of the organic interlayer. When the samples are imaged without any preparation, the organic layer can be seen sagging deeply between the cones. The sag was used to estimate the strength of the wet layer, considering that only its weight is acting on it. This resulted in extremely low values of the flow stress, suggesting that the organic is viscoelastic and flows under its weight when removed from water, which supports it under normal growth conditions. In stark contrast with these initial measurements (Meyers et al., 2008b), the nanoindentation method was used to penetrate the dry organic layer (Meyers et al., 2009) and encountered considerable resistance. This was a trial-and-error procedure in which the Berkovich indenter was lowered and touched, in a large fraction of the attempts, the organic layer. The configuration used in testing is shown in Fig. 13. One considers that the membrane is held up by three growth cones. When the Berkovich tip with a triangular base and angle of 136° is lowered, it may touch the organic before it encounters the mineral, situations depicted in Fig. 13(b) and (c). In this case, the load-penetration curve shows drastic changes from the ones in which the tips of the cones are encountered first. Actual curves are shown in Fig. 14. Fig. 14(a) shows that the force rises rapidly as the tip of the two cones are deformed. In one of the cases, the tip breaks, creating a characteristic displacement. For the

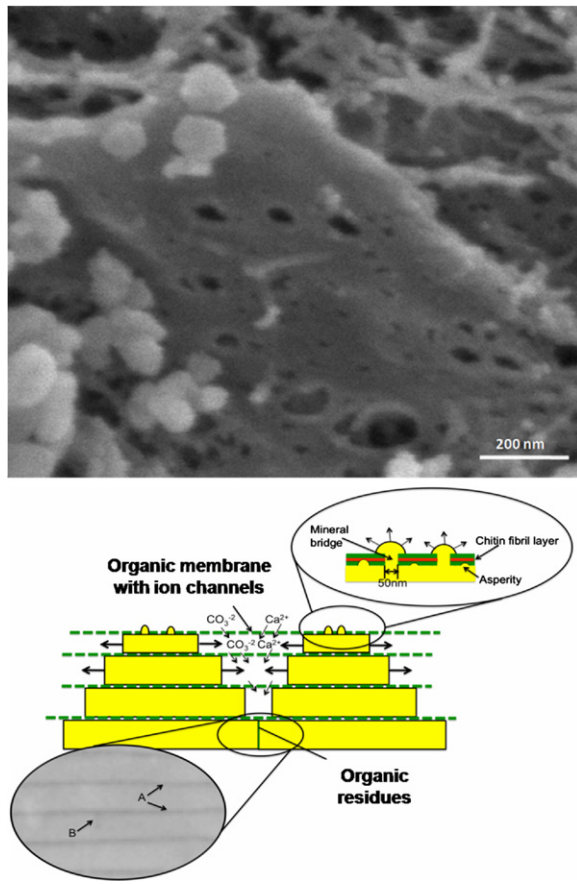


Fig. 11 – (a) SEM image showing thin intertile organic layer with holes ; (b) Proposed mechanism (Lin and Meyers, 2005, MSEA; Meyers et al., 2009, MSEC) of growth of nacreous tiles by formation of mineral bridges; organic layer is permeable to calcium and carbonate ions which nourish lateral growth as periodic secretion and deposition of the organic intertile membranes restricts their flux to the lateral growth surfaces. In inset (SEM Backscattering mode) the intertile organic layer is visible as dark horizontal lines (A), while regions where tiles abutt (vertical lines) are barely seen (B), supporting formation of interlayer organic layers to regulate growth.

Source: (a) From Lopez et al., MSEC (in press) (b) Adapted from Meyers et al., MSEC (2009).

other situation (Fig. 14(b)), there is a plateau at $P \sim 100 \mu\text{N}$, corresponding to the resistance of the organic layer. This penetration proceeds, for three curves, for approximately 300 nm. Considering some sag in the organic layer, this number represents one tile layer. One of the curves has a more extensive plateau, around 600 nm. In this case, it is thought that the indenter travels the distance of two layers, as shown in Fig. 13(c). These measurements were used to estimate the resistance of the organic layer to deformation and/or failure. There was a drastic increase in strength from the original values obtained by measuring the sag in the membrane, attributed to the high sensitivity of the structure on the degree of hydration. This is still an area of research

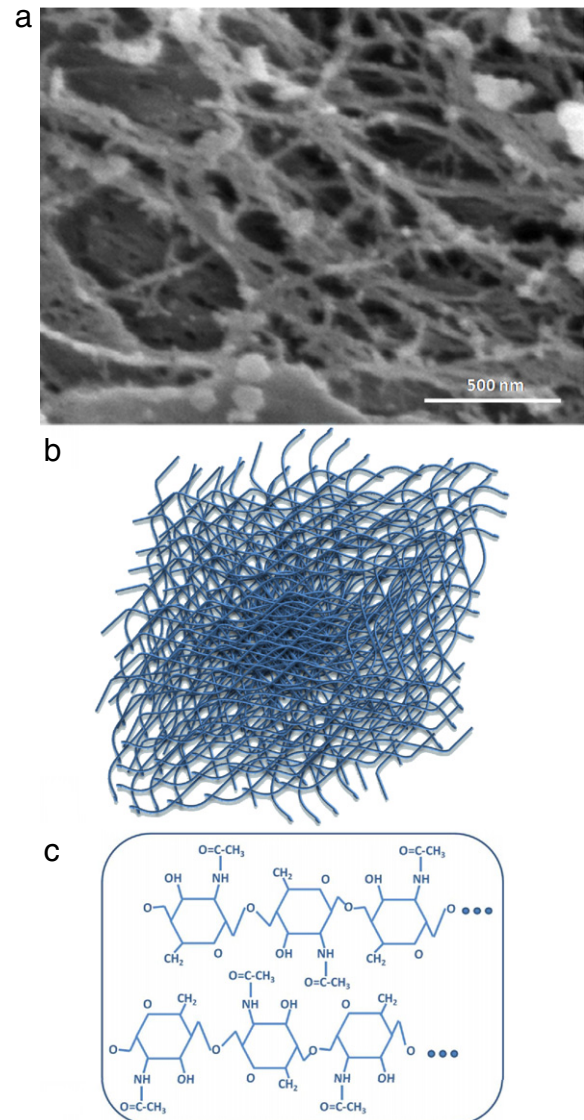


Fig. 12 – (a) Demineralized shell revealing randomly oriented chitin fibrils from intertile layers; (b) schematic representation of organic intertile layer composed of chitin fibrils; (c) chemical structure of chitin.

Source: Adapted from Lopez et al., MSEC (in press).

where more detailed analysis is needed to establish the effect of the organic layer hydration on its mechanical response.

How does the abalone produce the organic interlayer at periodic intervals? We excised a portion of the mantle, and examined its section, and particularly the region in close contact with the growth surface. Observation of the inner layer of the epithelium, which is only separated from the growth front by the extrapallial layer, revealed interesting features. This epithelium contains arrays of channels, Fig. 15(a). In some of these channels a few fibrils are seen and marked with arrows. Thus, one can envisage the synthesis of chitin in the channels and its periodic extraction/extrusion from there onto the growth front. Such a situation is depicted in Fig. 15(b).

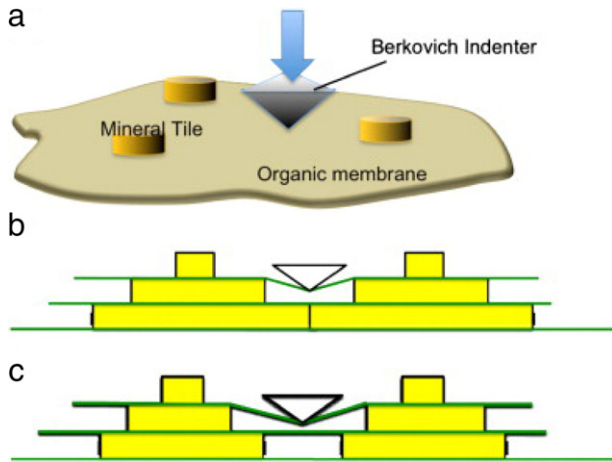


Fig. 13 – Representation of nanoindenter deforming organic layer; (a) tridimensional representation of indenter deforming organic layer; (b) configuration of a single organic layer with a mineral underneath; (c) configuration of an organic layer that is joined with lower level by deflection.

Source: Adapted from Meyers et al., MSEC (2009).

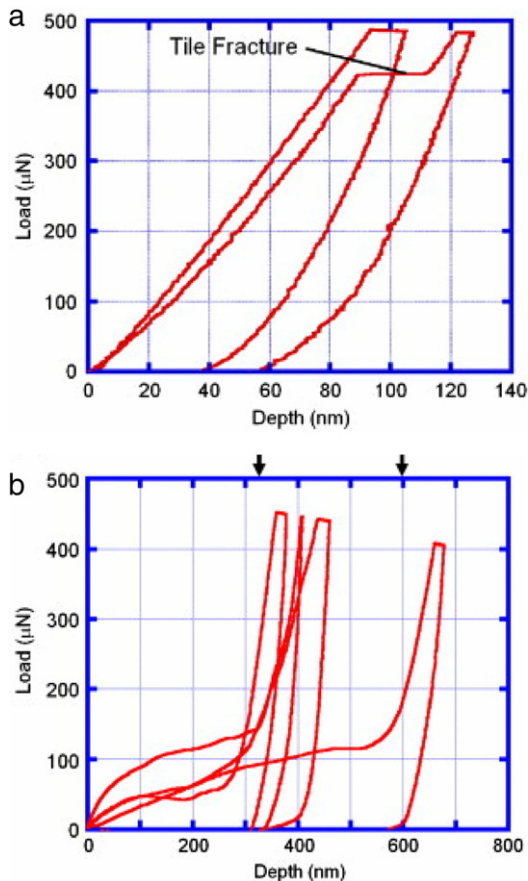


Fig. 14 – Nanoindentation load–displacement curves for (a) completely mineralized region and (b) organic layer in green abalone; notice the penetration for ~400 nm in three curves at a low load, before the indenter touches the mineral.

Source: Adapted from Meyers et al., MSEC (2009).

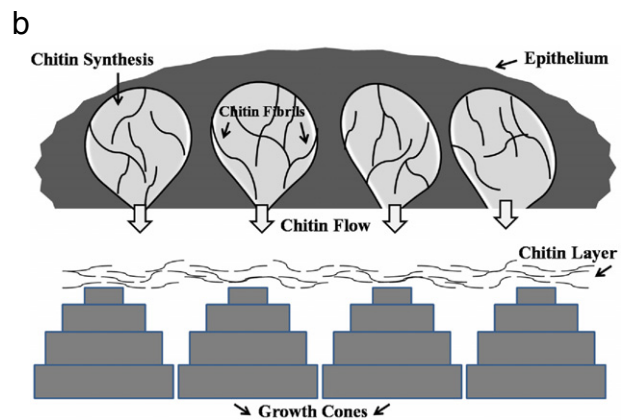
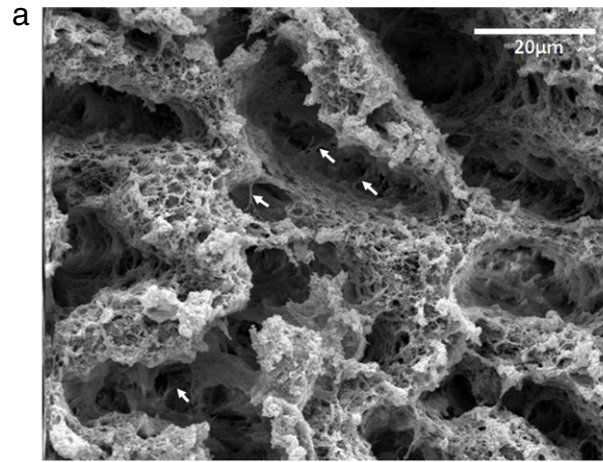


Fig. 15 – (a) Cross-section of epithelium with array of channels and occasional chitin fibrils (marked by arrow); (b) schematic depicting hypothetical mechanism by which epithelium generates chitin fibrils and 'squeezes' them onto growth surface.

Source: Adapted from Lopez et al., MSEC (in press).

The detailed knowledge of the structure at the different hierarchical levels is essential for the understanding of the mechanical properties of nacre. Gao et al. (2003) proposed that, at the nanoscale, the material can reach its theoretical strength because the crack is reduced to the size which is dictated by the scale. This is easily seen by the simplified plot in Fig. 16(a), which shows the stress required to propagate a crack in calcium carbonate, with a fracture toughness $K_{IC} = 1 \text{ MPa m}^{1/2}$. This curve intersects the line marking the theoretical cleavage stress, approximated as $E/30$, for a characteristic size of 56 nm. If one looks at the sizes of the mineral bridges joining adjacent mineral layers (Fig. 16(b)), one sees that these are their approximate diameters. Four such bridges are marked by arrows. Fig. 16(c) shows the distribution of tensile strengths obtained by applying tensile loads as indicated in Fig. 16(c). They are astoundingly low, around 3 MPa (Fig. 16(d)). It will be shown below that this is consistent with the calculations based on the observed density of mineral bridges.

Only a small fraction of all asperities form bridges. Indeed, Song et al. (2002, 2003) measured the number of these bridges

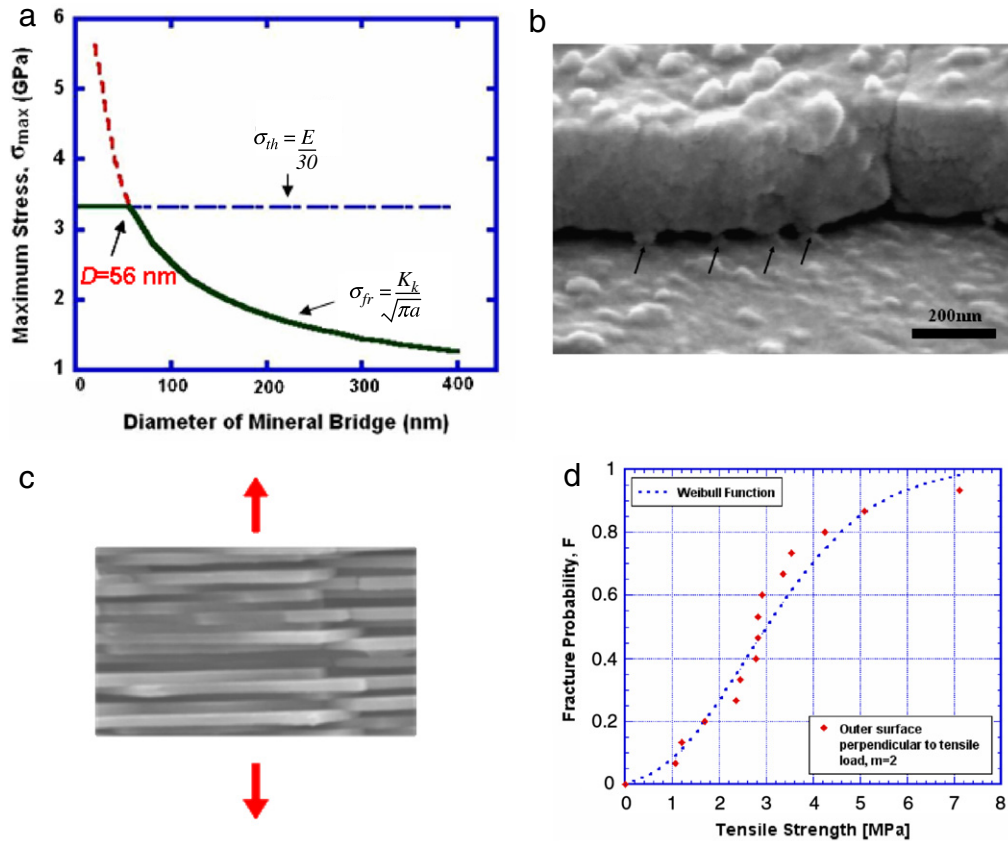


Fig. 16 – (a) Maximum fracture stress as a function of the diameter of the mineral bridge (critical flaw size); (b) SEM micrograph showing mineral bridges ~ 60 nm between aragonite tiles (marked by arrows) after deproteinization; (c) tensile testing direction perpendicular to tile layers; (d) tensile strength of shells perpendicular to layers.

Source: Adapted from Lin and Meyers, JMBBM (2009).

per tile and found approximately $n = 40$. These numbers are in agreement with the simple calculation shown here.

The tensile stress, σ_t , is equal to the sum of the forces exerted by n mineral bridges divided by the area of a tile, A_t . The force per bridge is equal to the theoretical stress, σ_{th} , multiplied by the bridge area, A_b . Thus:

$$\sigma_t = \frac{nA_b\sigma_{th}}{A_t}. \quad (5)$$

Taking the tile radius as $5 \mu\text{m}$, the number $n = 40$, the theoretical strength (Fig. 16(a)) $\sigma_{th} = 3.2$ GPa, and the diameter of the bridges equal to 60 nm, one obtains:

$$\sigma_t = 1.2 \text{ MPa}.$$

This is on the same order of magnitude as the mean from the Weibull distribution in Fig. 16(d) ($\sigma_t = 3$ MPa). One can also expect the organic layer to contribute with bonding between adjacent layers. It should be mentioned that Kamat et al. (2000, 2004) took exception to the Gao et al. (2003) analysis. They attributed the strength to micrometer-scale features.

These results are indeed significant and indicate that the mineral bridges play a seminal role in the mechanical properties of the abalone shell. Lin and Meyers (2009) extended this treatment to the tensile and shear strength and obtained consistent values. The most important attribute of nacre, its high toughness, is a direct result of the relatively

large tensile strength when pulled along the direction of the tiles. We recognize that the shell is not subjected to tension in this direction in its natural habitat. Nevertheless, tension is involved in bending, a stress that is definitely involved when a predator pries it from a rock. Flexure tests show values of 170 MPa, compared with a compressive strength of 235 MPa, in the same orientation. Dog-bone shaped samples were also used to determine the tensile strength of nacre when loaded parallel to the plane of growth; the mean strength was considerably lower, 65 MPa. Nevertheless, the tensile strength is a much higher fraction of the compressive strength ($1/4$ – $1/2$) than in monolithic ceramics, where it fluctuates between $1/10$ and $1/15$. The failure occurs by the process shown in the SEM micrograph of Fig. 17(a): the tiles pull out and are only occasionally broken. On the other hand, if the bonding between tiles were stronger, they would crack and allow the propagation of a crack that could cross the specimen unimpeded. Shear tests were conducted on a special fixture with a shear gap of $200 \mu\text{m}$, approximately $100 \mu\text{m}$ narrower than the spacing between mesolayers. Fig. 17(b) shows how the tiles slide past each other. Assuming that the majority of failure occurs through tile pull-out and not through tile fracture, the tensile strength can be converted into shear strength. Indeed, we measured the average pull-out strength of tile segments in tension (Lin and Meyers, 2009).

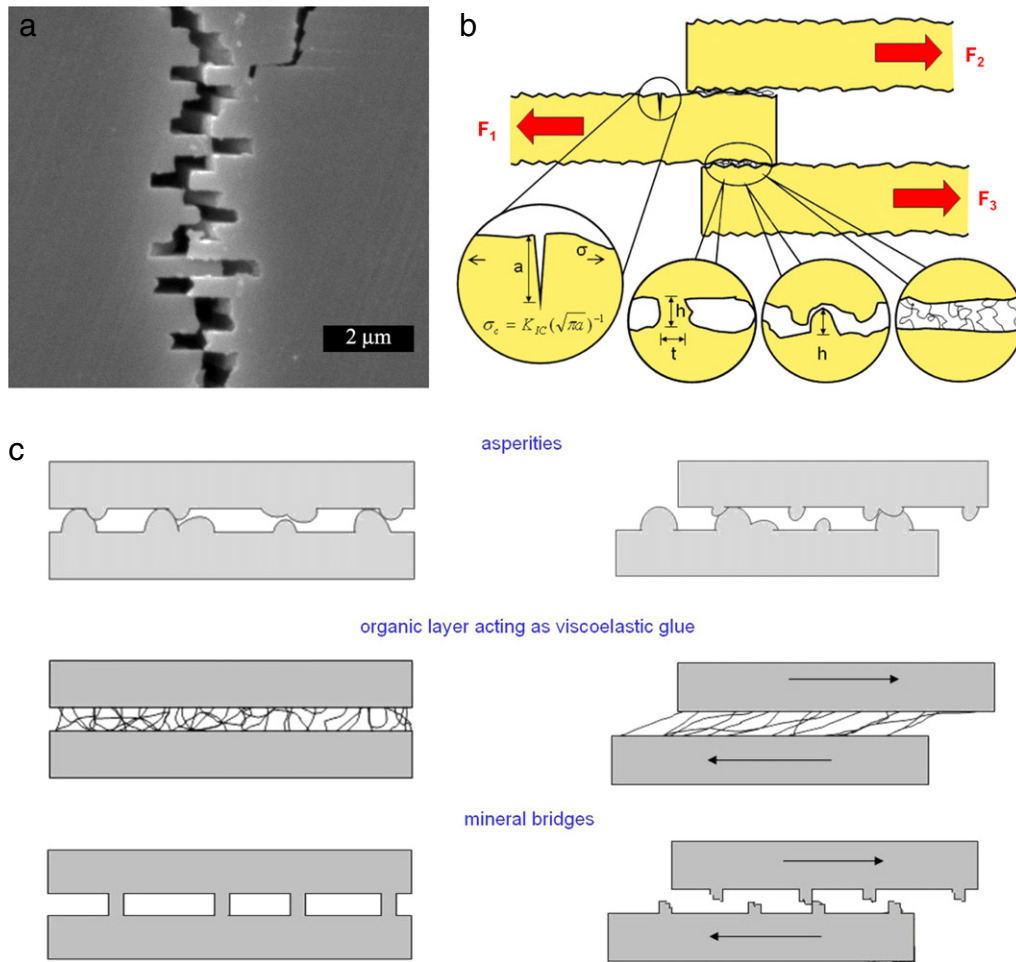


Fig. 17 – Origin of toughening in nacre: (a) SEM micrograph showing sliding of tiles in tensile loading; (b) balance between tile fracture and intertile shear; (c) details of three mechanisms of intertile shear: asperities, organic layer acting as viscoelastic glue, and fracture of mineral bridges.

Source: Adapted from Lin and Meyers, *JMBBM* (2009).

There are three principal mechanisms contributing to the strength of the abalone shell, shown in the insets of Fig. 17(b): mineral bridge breaking, asperities, and the bonding provided by the organic interlayer. These three mechanisms are shown in more detail in Fig. 17(c).

Taking the equilibrium of forces in Fig. 17(b) the relationship between the tensile stress on tile, σ_t , and shear stress on organic interfaces, τ_s , can be calculated for a simple two-dimensional case:

$$F_1 = F_2 + F_3 \quad (6)$$

$$\sigma_t t = 2\tau_s S \quad (7)$$

where σ_t is the tensile strength of the tile and τ_s is the shear strength of the intertile layer. S is the mean overlap between tiles and t the tile thickness. From Fig. 17(a) one can estimate the mean overlap between tiles: $S = 0.63 \mu\text{m}$. Their thickness is $t = 0.5 \mu\text{m}$. Thus, one obtains:

$$\sigma_t / \tau_s = 2S/t = 2.5. \quad (8)$$

For the abalone tile configuration, the tensile strength of the mineral should be at least equal to 2.5 times the shear strength of the interface to ensure shear failure by sliding.

The shear strength is found to be $36.9 \pm 15.8 \text{ MPa}$ with an average maximum shear strain of 0.3. Assuming a fracture toughness of $1 \text{ MPa m}^{1/2}$, one can obtain a critical crack size that will be arrested by the sliding of tiles.

In conclusion, the layered structure of the abalone shell provides anisotropy of mechanical strength that increases the toughness in a very significant manner by increasing the resistance to crack propagation perpendicular to the surface and decreasing it correspondingly parallel to it.

3.2. Toucan and hornbill beaks

Whereas birds usually have either short and thick beaks or long and thin beaks, toucans have long and thick beaks. The Toco Toucan (*Ramphastos toco*) has the largest beak among the species. The large beaks help in picking up fruits at the tips of branches in the canopy and extracting prey (little baby birds!) from holes in trees. They also assist in combat and bill fencing. The Toucan beak is one-third of total length of the bird; nevertheless the weight is 1/30th–1/40th of its mass. The African Hornbill also has an extraordinarily large beak; it is, however, heavier. This is accomplished by an ingenious

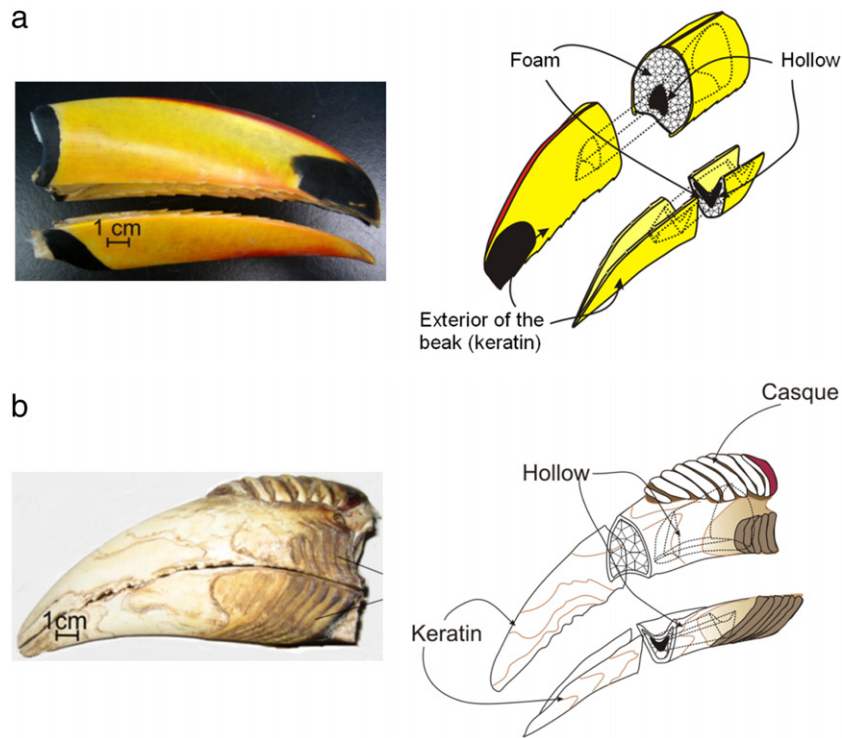


Fig. 18 – Photographs and schematic drawings of (a) toucan and (b) hornbill beaks.

Source: (a) Adapted from Seki et al., *Acta Mater.* (2005), (b) Adapted from Seki et al., *Acta Biomater.* (2010).

solution, enabling a low density and sufficient rigidity. The outside shell (integument) of the beak consists of β -keratin, that is typically found in avian and reptilian species. The inside is filled with a cellular bone. This internal foam has a closed-cell structure constructed from bony struts with thin membranes.

Fig. 18 shows photographs and schematics of the toucan and hornbill beaks. This structure was found by Seki et al. (2005) to have a maximum bending moment (Brazier moment) that is considerably higher than if all the mass were concentrated in the shell as a solid hollow cylinder by applying the analysis developed by Karam and Gibson (1995). Seki et al. (2005, 2006) showed that the internal cellular core serves to increase the buckling resistance of the beak and demonstrated a synergism between the two components that provides the stability in bending configuration. Thus, there is clearly an advantage in having an internal foam to support the shell. The nature of the internal foam structure is revealed in considerable detail by micro-computerized tomography. Fig. 19 shows both longitudinal and cross-sections of the internal foam. The cell sizes are of the order of 1 mm. The mechanical properties of the shell are measured along the longitudinal and transverse directions and are found to be anisotropic (Fig. 20(a)). The compressive strength of the foam was established (Fig. 20(b)). It was found, as predicted, that the foam in the hornbill is much stronger, by virtue of its higher density. In order to model the beak foam by FEM, its compressive behavior was first evaluated; we further performed tensile and compression testing on the trabeculae and the cortical shell to obtain the mechanical properties of the foam material. Although the cortical shell

and trabecular rods are made from the same materials, we measured the mechanical properties separately to take into account the anisotropy of the trabeculae and cortical shell. For obtaining the response to stresses of the foam at the level of the bone fibers, individual struts were tested in both tension and compression. Beak trabeculae from the inner cellular structure were sectioned from beak foam by razor blade. The cross-section of trabeculae is elliptical or circular; dimensions are typically $\sim 200 \mu\text{m}$ in diameter and $\sim 1.6 \text{ mm}$ in gauge length. The trabeculae were affixed in polymer resin mold that was allowed to harden and tested under tension as shown in Fig. 21(a). For compression, the trabeculae were glued onto metal plates and tested as shown in Fig. 21(b). Dimensions of compression samples varied from 2.5 to 4.5 mm in gauge length; 0.09 to 0.16 mm in thickness; and 0.12 to 0.28 mm in width. An Instron Model 3342 with 500 N load cell and cross-head speed of 0.05 mm/min was used for the trabeculae. The specimens fractured at the edge were removed from the sampling to eliminate the effect of the adhesive. Young's modulus obtained from twenty-five tensile tests of trabeculae is $3.0 \pm 2.2 \text{ GPa}$. The tensile strength was well described by a Weibull distribution with a characteristic strength, $\sigma_0 = 97 \text{ MPa}$ (Fig. 22(a)). The compressive tests produced buckling of the struts. The response of the struts is well described by the classic Euler equation for columns subjected to compression (Fig. 22(b)); the results fluctuate somewhat between fixed and pinned ends. The structure of shell and foam are imported and converted into meshes as shown in Fig. 23. The FEM simulation of the response of the beak was implemented by separating the shell and the interior, importing the microstructure of the bony foam with

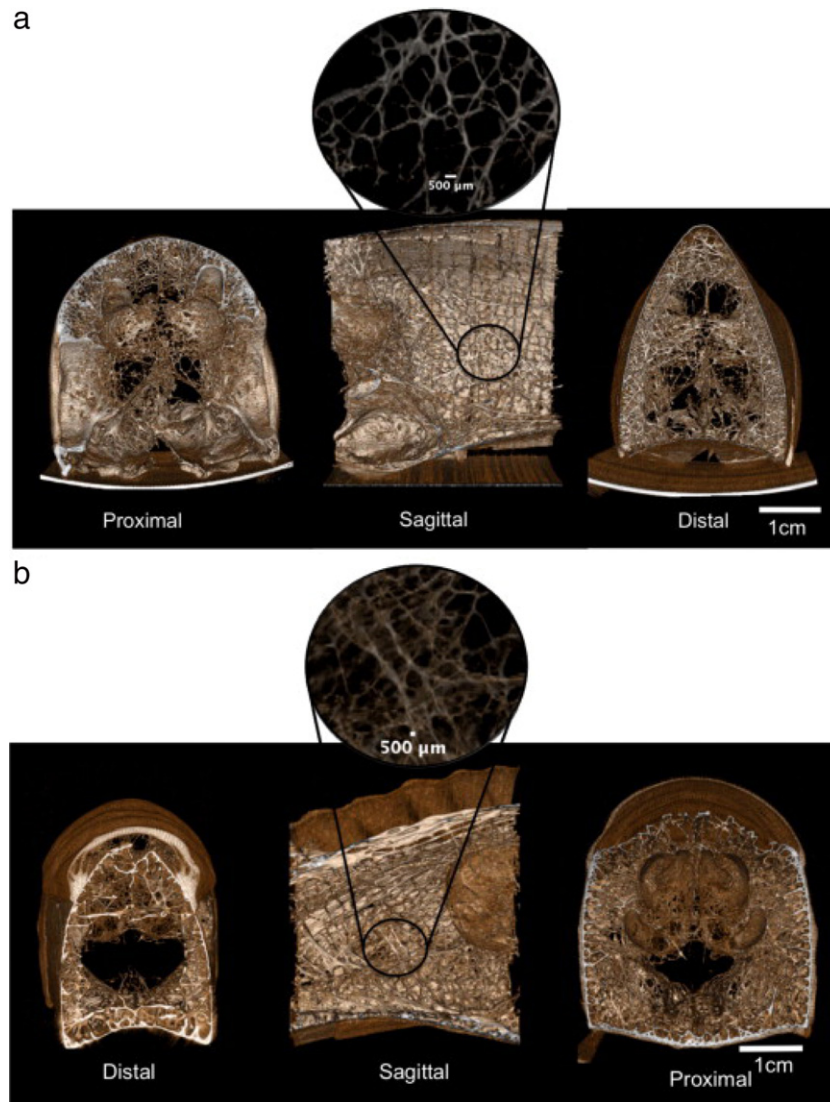


Fig. 19 – Three-dimensional structure of foam generated by VTK at distal and proximal cross-sections as well as a sagittal view of the mid-region from μ -CT scans for: (a) toucan and (b) hornbill.

Source: Adapted from Seki et al., *Acta Biomater.* (2010).

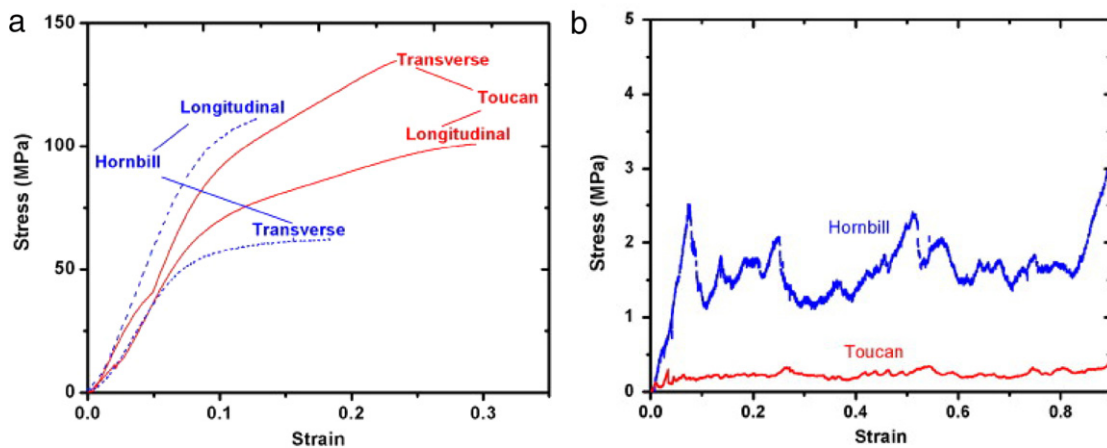


Fig. 20 – Representative stress–strain curves for toucan and hornbill beaks: (a) external keratin (rhamphotheca) in tension; (b) internal foam in compression.

Source: Adapted from Seki et al., *Acta Biomater.* (2010).

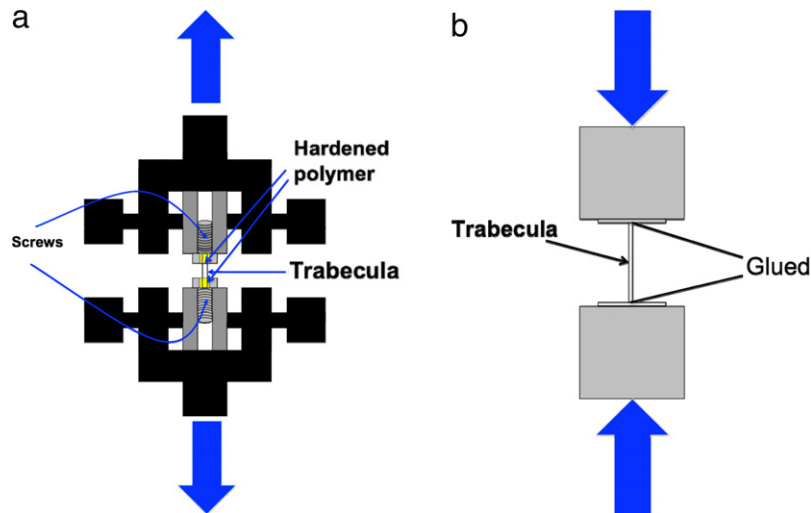


Fig. 21 – Mechanical testing procedure for trabeculae; (a) tensile and (b) compressive tests.

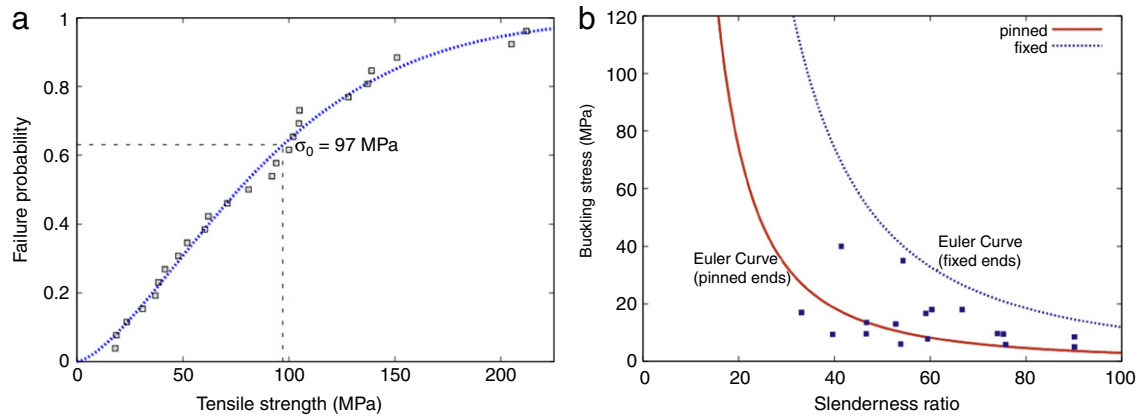


Fig. 22 – Mechanical testing of individual bone fibers from cellular structure; (a) Weibull distribution from tension; (b) Euler curves (buckling stress versus slenderness ratio), results from tensile and compression testing.

a 93 μm resolution, and by bringing together and assembling the two components, as shown in Fig. 23.

The strength of the shell, shown in Fig. 20(a) and that of the bony struts served as input for the modeling effort, whose results are illustrated in Fig. 24. This enables the simulation of the compressive deformation of a segment of the beak. The results of the simulation (Fig. 24(a)) are compared with actual experiment (Fig. 24(b)) and it is found that the FEM model captures the most important aspects of the deformation process, including the buckling and tearing of the shell. Thus, a rigorous analysis coupled with the local mechanical property collection can simulate the response of the beak. This study is in line with current efforts focusing on cancellous and compact bone using mechanical properties at the small scale and capturing the details of the deformation and failure process (Rietbergen et al., 1995; Müller and Rügsegger, 1995; Ulrich et al., 1998; Borah et al., 2001; Nagaraja et al., 2004). Figs. 25 and 26, respectively, show the separate responses of the shell and cellular bone interior to compression. The shell readily collapses by buckling in

Fig. 25(c). The combined action of the two components leads to the synergy observed in the beak and depicted in Fig. 27. One sees in a clear fashion that shell+foam is stronger than the sum of shell and foam compressed separately.

Sandwich composites can be found not only in nature but also in engineering materials. Gibson and Ashby (1997) describe a number of synthetic sandwich structures. There are polyurethane foams (self-skinning) with higher density on the outer surface and lower density in the core. Most engineering sandwich panels are made from a high-modulus face material and a low-modulus foam core. Hence, the toucan beak presents a novel approach to the design of these structures. Recently, a new class of materials, metallic foam, has been introduced and applied to make sandwich panels that have superior properties to polymeric foams. In synthetic sandwich panels, the combination of foam core and face materials is selected as a compromise between cost and performance. Despite these developments, the sandwich composites in nature are still far beyond the man-made constructions in terms of functionalities and optimization.

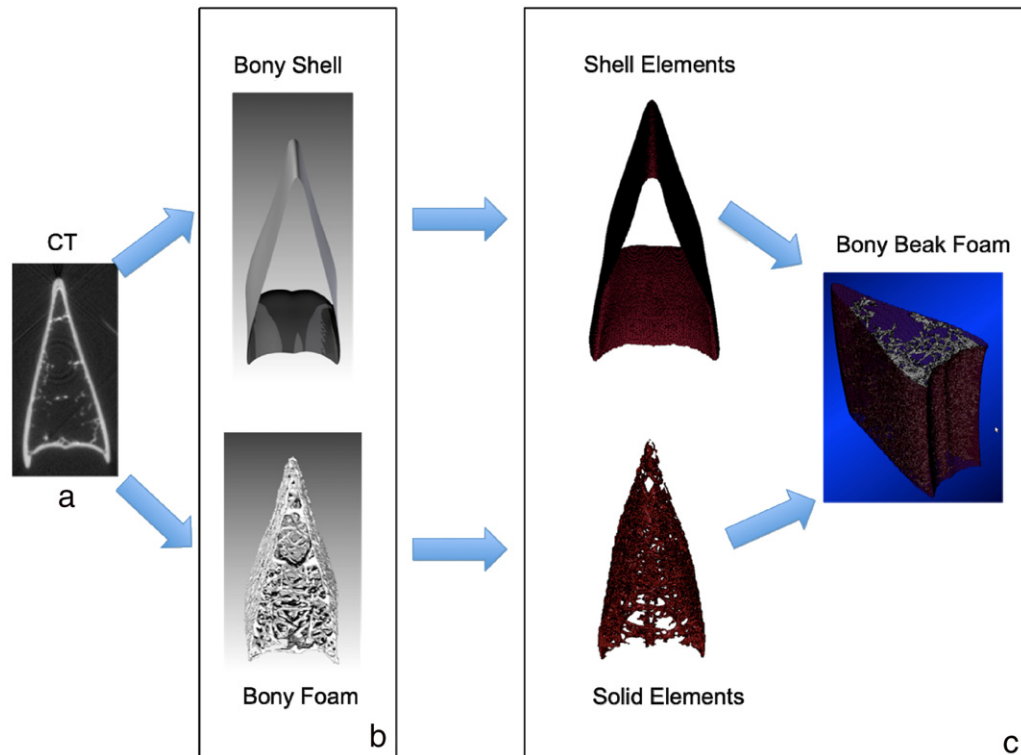


Fig. 23 – Conversion of CT images to FE model; (a) CT image, scanned with a resolution of 93 μm ; (b) tridimensional rendering of bony foam and shell; (c) FE model of shell and foam, finally assembled to create bony beak foam.

4. Functional biological materials

Biological materials exhibit a range of functional properties, which have been extensively studied in the past years. Noteworthy are the optical properties of the hexactinellid sponge, that act as optical fibers; the brittle star, an echinoderm, changes color from black (during day) to white (at night) (Aizenberg, 2010); the iridescence of butterflies, related to the nanostructure of the wing; the chameleon skin, that changes its color; the generation of current in electric eels; the magnetic oxides embedded in the brains of pigeons that act as guidance systems.

We focus here on one functional property, the ability to attach to surfaces. Barnacles (Berglin and Gatenholm, 2003) and mussels (Waite and Tanzer, 1981; Waite, 1987; Bell and Gasoline, 1996) attach in a permanent manner through intricate processes involving chemistry. However, a number of animals have evolved reusable attachment devices: insects, lizards, frogs. Barnes (2007) classifies attachment devices in animals into:

- **Interlocking:** Interlocking is the mechanism by which felines climb trees. This is a strictly mechanical process and can be accomplished by penetrating the surface with sharp claws.
- **Friction:** Friction consists of the micro-interlocking of the surfaces because of their roughness and intermolecular forces between materials and requires an angle that is below 90° .
- **Bonding:** it involves the formation of bonds between the animal and the surface and has three possible

mechanisms acting separately or together: wet adhesion (capillarity), dry adhesion (van der Waals), and suction (through reduced internal pressure).

We will illustrate these concepts through three examples: the gecko, the tree frog (*Scynax perereca*), and the abalone foot.

4.1. The gecko foot

The gecko is the stellar example of an animal that can apparently defy gravity by using a unique structure in the foot pad. It is well known and intensively studied. However, the mechanism by which it attaches itself is not unique. Flies, bugs, and other taxa have developed similar devices. Fig. 28(a) shows a common ladybug attached onto a flower. Fig. 28(b) is a SEM micrograph showing a retracted foot. One should notice that the ladybug has quite hairy legs. Upon observation at a higher magnification (Fig. 28(c)), it is apparent that the foot contains thin cylindrical rods, called setae, terminating in spatulae, with diameters of $\sim 2 \mu\text{m}$. These spatulae attach to surfaces through van der Waals forces.

In the case of the gecko, which has a much bigger mass, the setae and spatulae are equally observed. A principal difference is the greater extent to which the setae split into spatulae, with diameters of $\sim 100 \text{ nm}$. The setae are arranged bundles which have a regular pattern with channels between them. These bundles have an approximate square shape with $10 \mu\text{m}$ side. Fig. 29 shows this in a clear manner. These bundles terminate at a common source and have a length of $\sim 100 \mu\text{m}$. The distal ends of the setae split up into a large number of fibrils. The terminations, called spatulae, have

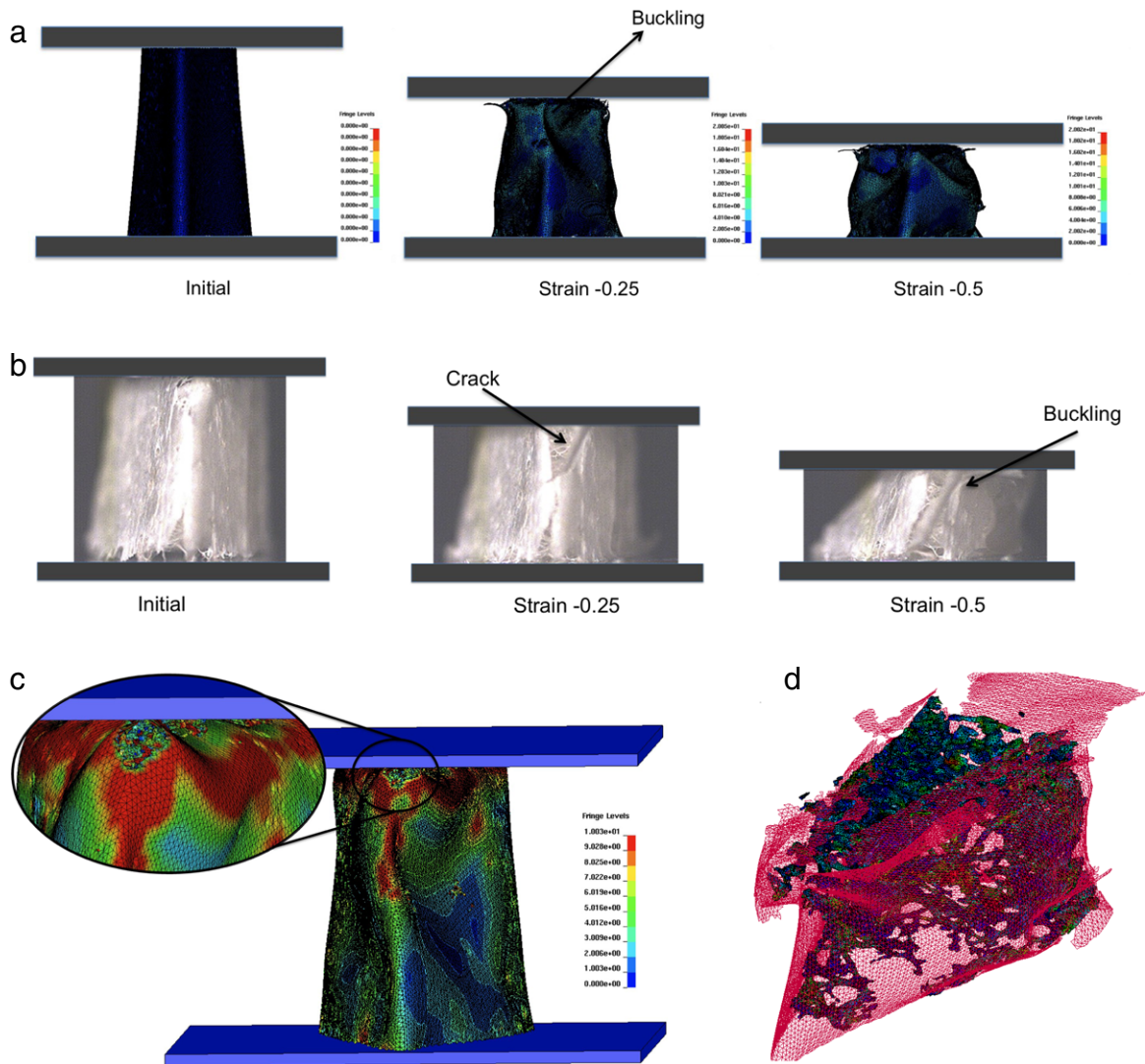


Fig. 24 – Comparison of experiment and FEA; (a) deformation of foam in FEM calculation at strains of 0, –0.25, –0.5; (b) deformation of foam in experiment at strains of 0, –0.25, –0.5 strain; (c) cortical shell splitting in FEA at –0.1 strain; (d) FEM calculation at –0.5 strain, showing that the bony exterior is locally buckled and fractured.

diameters between 50 and 120 nm. The scale of the gecko spatulae is one order of magnitude lower than that of the ladybug.

Arzt et al. (2003) and Huber et al. (2005) calculated the stress required to pull off a contact and explained the scale effect. This calculation is based on the van der Waals forces combined with Hertzian contact stresses. For simplicity, spatulae are assumed to have semi-spherical extremities, as a first approximation. The contact radius, a , for a spherical cap of radius R in contact with a flat surface and subjected to a compressive force F is, according to Hertzian elasticity (e.g., Ugal and Fenster, 1987):

$$a = 0.88 \left(\frac{2RF}{E^*} \right)^{1/2}. \quad (9)$$

Johnson et al. (1971) inserted the attractive force between the two bodies and obtained the expression (as quoted by Arzt, 2006):

$$F = \frac{4}{3} E^* \frac{a^3}{R} - (4\pi E^* \gamma a)^{1/2} \quad (10)$$

where γ is the work of adhesion of the two surfaces that produces the van der Waals force. The critical radius of contact a_c is obtained by taking:

$$\frac{\partial F}{\partial a} = 0. \quad (11)$$

This leads to

$$F_c = \frac{3}{2} \pi R \gamma. \quad (12)$$

This result is, surprisingly, independent of E . More complex analyses incorporate the elastic constants. In the case of attachments, only a fraction of the surface, f , is covered by spatulae. The adhesion stress can be computed from F_c considering the area of contact of each spatula to be equal to πR^2 . The stress required to pull off a spatula is the force F divided by the apparent area,

$$\sigma_{app} = \frac{3 f \gamma}{2 R} \quad (13)$$

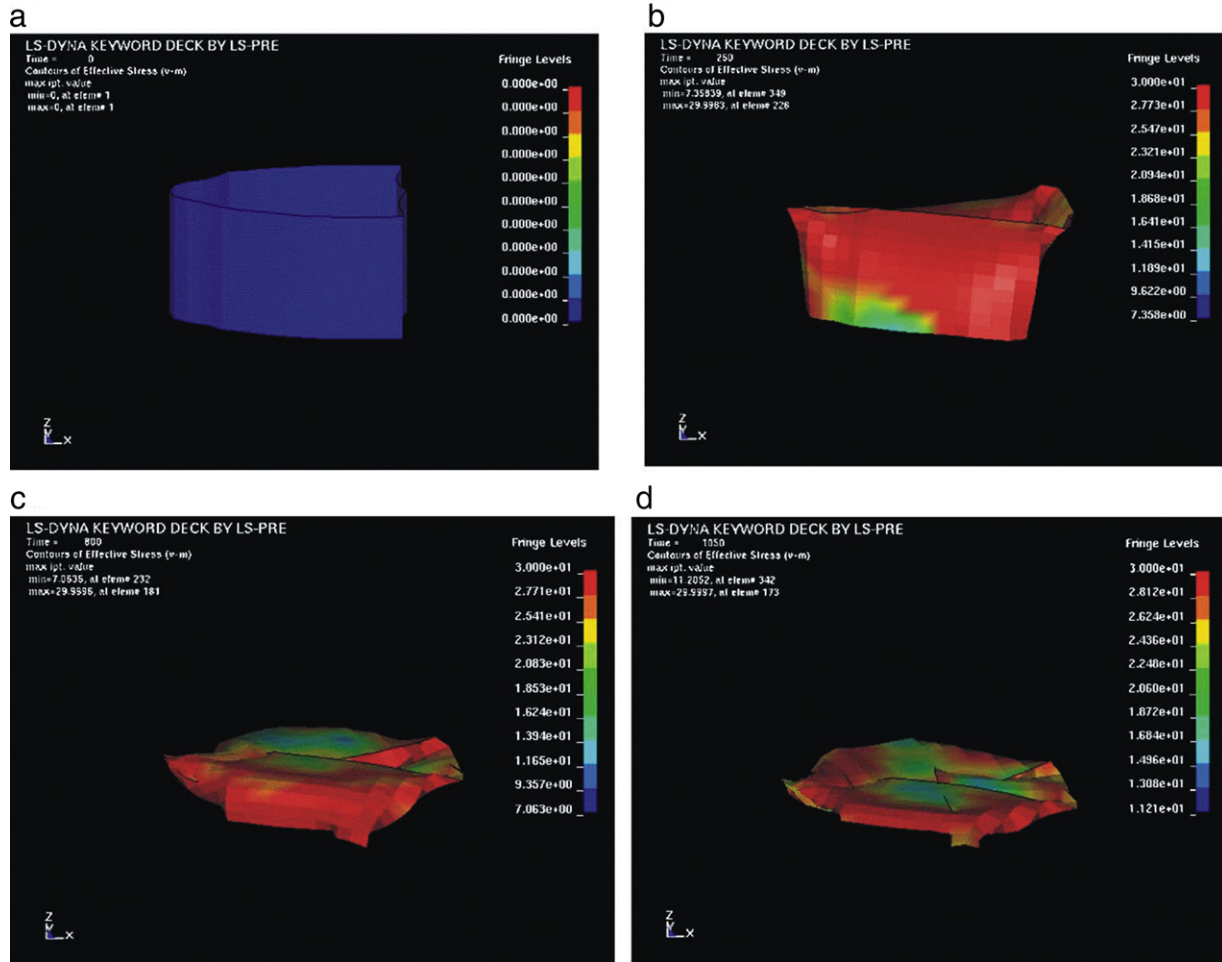


Fig. 25 – FEM simulation of the beak shell under compression testing; (a) FEM model of shell; (b) onset of folding; (c) buckled shell; (d) completely collapsed shell.

Source: Adapted from Seki et al., MSEC (2006).

where f , the fraction of the area covered by setae, is

$$f = \frac{\pi R^2}{A_{app}} \quad (14)$$

It can be seen that the pull-off stress in Eq. (13) is inversely proportional to R . Thus, the larger the mass of the biological system, the smaller R has to be. For geckos, that have a mass of approximately 100 g, it is equal to 10 setae per μm^2 . The ladybug, on the other hand, has a mass of ~ 0.2 g and a density of 0.05–0.2 setae per μm^2 . It should be mentioned that for extremities that are not semi-spherical other relations apply, as will be seen under Section 5.

4.2. Tree frog

The toe pad of the Brazilian tree frog (*Scynax perereca*) provides a splendid example of functional adhesion in nature. This animal, which lives in the moist environment of the subtropical rain forest, is able to jump from surface to surface, and attach itself effectively through a variety of electro/mechanical/chemical actions employed by the materials at the surface of its toe. Its movements are much more dynamic than the gecko. We observed that the toe pad

of the Brazilian tree frog is also, and surprisingly, composed of aligned nanoscale fibrils. The fibrils are sectioned into highly ordered hexagonal bundles (Lin, 2008). These bundles, described first by Ernst (1973a,b); Welsh et al. (1974) and studied later by many others (Green, 1979; McAllister and Channing, 1983; Green and Simon, 1986) are separated by canal-like grooves. More recent studies have been carried out by Hanna and Barnes (1991) and Barnes et al. (2005, 2006).

The structure of the toe pad is depicted in the schematic diagram presented in Fig. 30. The diagram shows a tree frog attached to a glass substrate, with an illustration of the hexagonal subdivisions approximately 10 μm in diameter. These subdivisions are comprised of closely packed fibers approximately 100 nm in diameter. Each fiber terminates in cups of approximately 200 nm diameter (Lin, 2008). Each one of these cups is aligned beside its neighbor forming a flat surface. Fig. 31 provides a scanning electron micrograph of a single toe at low magnification with an expanded view of the surface of the toe pad showing hexagonal subdivisions. A well defined circular pad of roughly 2.5 mm in diameter can be seen at the center of the toe. This area represents the surface of thousands of well packed pseudo-hexagonal bundles as seen in the expanded caption of the figure.

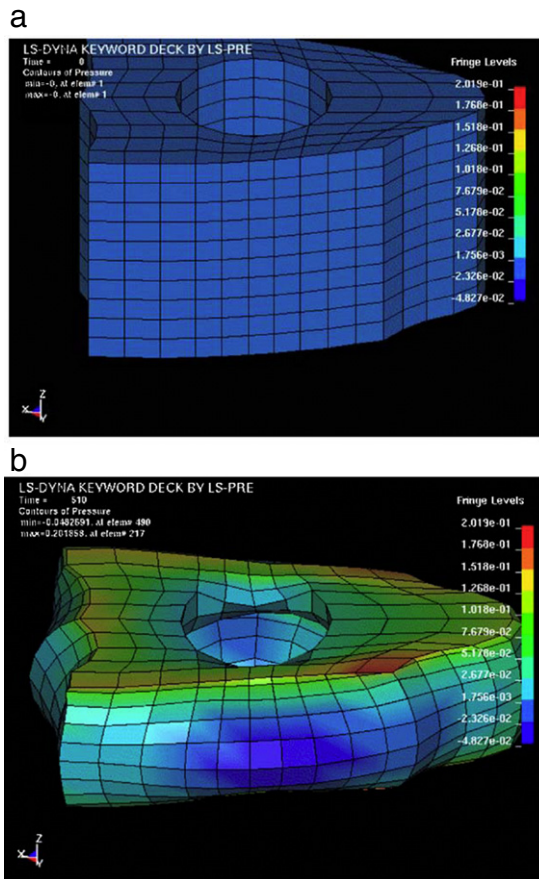


Fig. 26 – FEM modeling of foam under uniaxial compression testing; (a) undeformed foam; (b) deformed foam.

Source: Adapted from Seki et al., MSEC (2006).

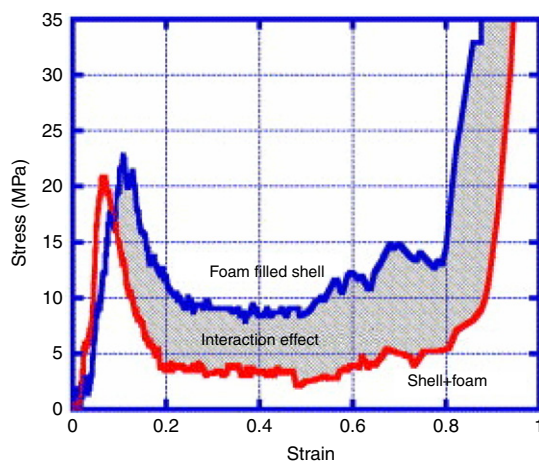


Fig. 27 – Compressive stress–strain curves of foam + shell and foam filled shell which show strong synergistic effect.
Source: Adapted from Seki et al., Acta Mater. (2005).

Barnes (2007) reported that the mucous glands excrete a viscous fluid which can be transported through the canals

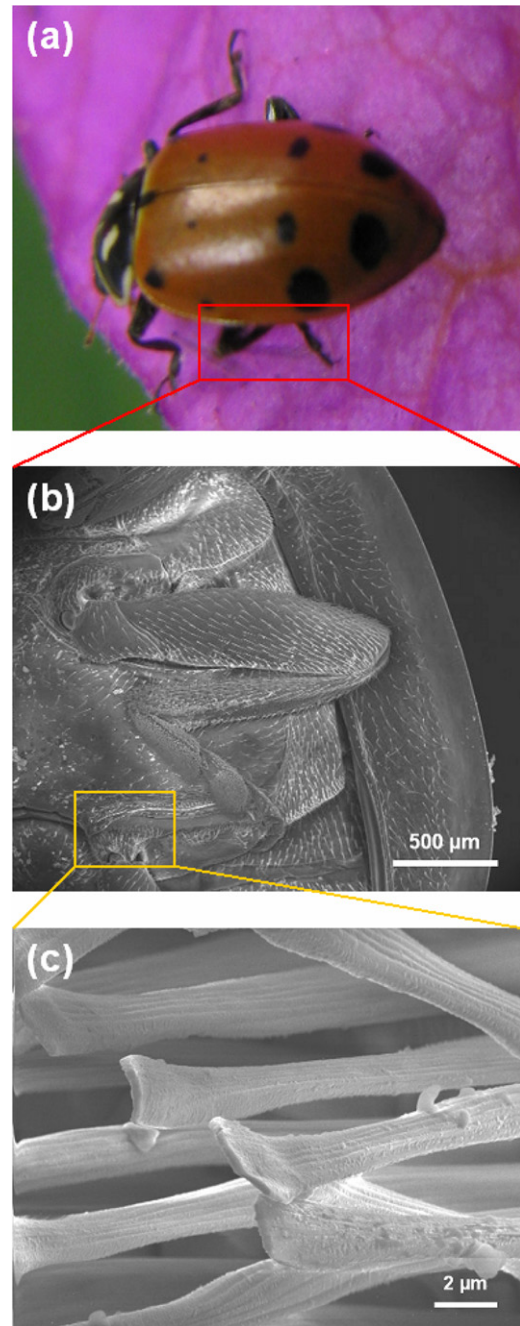


Fig. 28 – Ladybug attachment devices: (a) ladybug; (b) retracted foot; (c) setae terminating in spatula.

that exist between the hexagonal subsections. It had been suggested that the fluid plays an essential role in adhesion, indicating a domination of wet adhesion mechanism. It is proposed here that the contribution of molecular adhesion through van der Waals interactions between the nanofibril ends and a surface may have a place in the discussion of tree frog toe pad adhesion.

Fig. 32 provides (a) top-down, and (b) cross-sectional view of an individual bundle. The tightly packed, well aligned fibers which comprise these bundles are shown in greater detail in Fig. 33. The terminating cups on neighboring fibers are

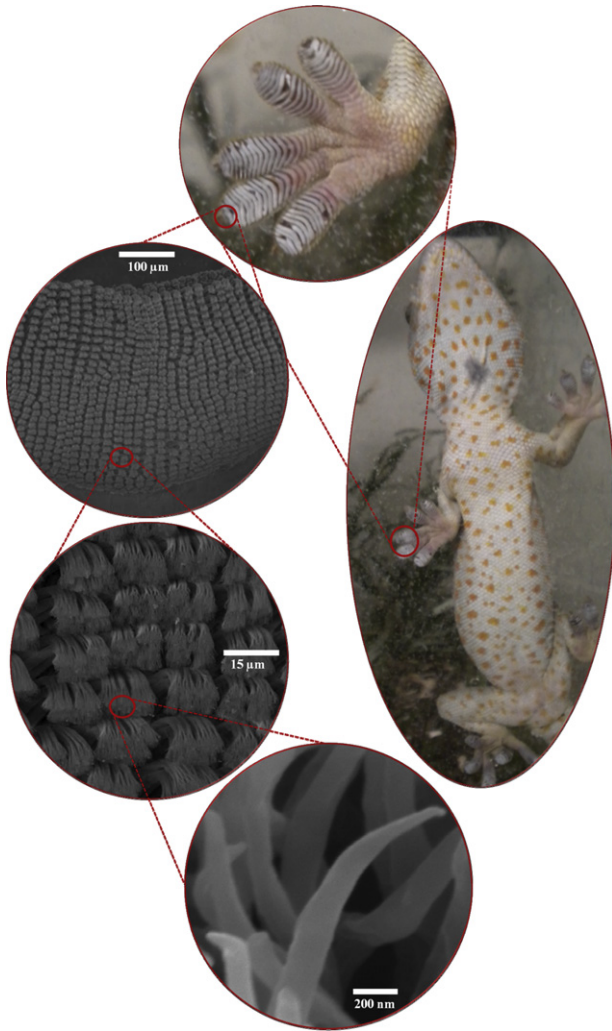


Fig. 29 – Gecko and structure of attachment shown at increasing magnifications, starting with setae in rectangular arrays terminating in spatulae with diameters of approximately 100 nm.

aligned closely against each other to create a smooth and consistent surface.

4.3. Abalone foot attachment

Our group has extended the study of the structure of abalone to the attachment forces required to separate it from a surface (Lin et al., 2009). The detachment stresses were measured on live and healthy abalone and found to be of the order of 115 kPa. The pedal foot of red abalone (*Haliotis rufescens*) is shown in Fig. 34. The dark pedal folds, spaced approximately 0.5 mm apart, are the source of locomotion waves used in transportation (Trueman and Hodgson, 1990; Donovan and Carefoot, 1997). These locomotion waves have an analog in Materials Science in the dislocation. The fold in the pedal propagates along the foot, generating, after its passage, a displacement equal to the length of surface at fold. Fig. 34(b) shows an abalone supporting its own weight via a single contact point (a human finger). Fig. 35 shows a large magnification scanning electron microscopy

(SEM) image of the cross-section of the soft tissue. Folds can be seen in greater detail as a mechanism in which the surface area of the foot can expand and contract allowing an increase or decrease in contact surface area and providing the mechanism for the propagation of waves on the ventral surface of the pedal muscle.

At higher magnification, Fig. 36(a) shows setae lining the outer surface of the tissue with a thickness of 1–2 μm. At their extremities, (Fig. 36(b)) the setae separate into nanoscale probes with hemispherical ends (c), averaging 150 nm in diameter and uniaxially aligned perpendicular to the plane of the foot tissue. It is proposed that, as in the case of the gecko, these nanofibrils create intimate contacts at the molecular level to form van der Waals interactions which can be accumulated into a formidable macroscale effect. A close view showing the alignment of these nanofibrils is shown in Fig. 37.

The influence of a meniscus fluid between a fiber and a substrate is increasingly significant with decreased liquid–surface contact angle, i.e. a hydrophilic substrate would have more capillary interactions than a hydrophobic one. This is clearly seen in Fig. 38.

In the case of the hydrophobic material the average pull-off force was determined to be 294 nN, remaining constant under varying humidities. If one assumes that 60 nanofibrils on a single seta are in contact with the surface, this would correspond to an adhesion force of approximately 5 nN per nanofibril. This estimate is in exact agreement with the theoretical results of 5 nN calculated using the Johnson–Kendall–Roberts equation. When the seta was tested on a hydrophilic substrate, at a relative humidity of 10%, the pull-off force was observed to be 424 nN before detachment. This represents an increased force of 130 nN relative to test on the hydrophobic substrate, which can be partially explained by the variation in surface energies for the two substrates (20 mJ/m² and 55.5 mJ/m² for the disc and silicon oxide, respectively). However, raising the relative humidity to 67% resulted in an additional increase in pull-off force to 558 nN. Similar to predictions by Autumn et al. (2002) and work by Huber et al. (2005) for the gecko foot, this shows evidence of capillary interactions. The characterization of the abalone foot pedal and the mechanical tests suggest that the three mechanisms proposed by Barnes (2007) act cooperatively (and perhaps synergistically). Suction can generate attachment forces as explained schematically in Fig. 39 (a). It can be shown that the detachment force F_d is equal to:

$$F_d = PA \quad (15)$$

where P is the pressure and A is the projected area of the abalone foot on the plane of the surface of attachment. Assuming that the effect of the water column is negligible, i.e., $P = P_{atm}$, we obtain the mean attachment stress as,

$$\sigma_d = P_{atm} = 101 \text{ kPa}. \quad (16)$$

Fig. 39(b,c) show schematically how the three mechanisms can operate cooperatively to create the attachment stress on the same order of magnitude as the theoretical suction stress. The setae and nanofibrils maintain intimate contact with any irregular surface, closing possible channels and impeding water penetration. The pressure at the interface,

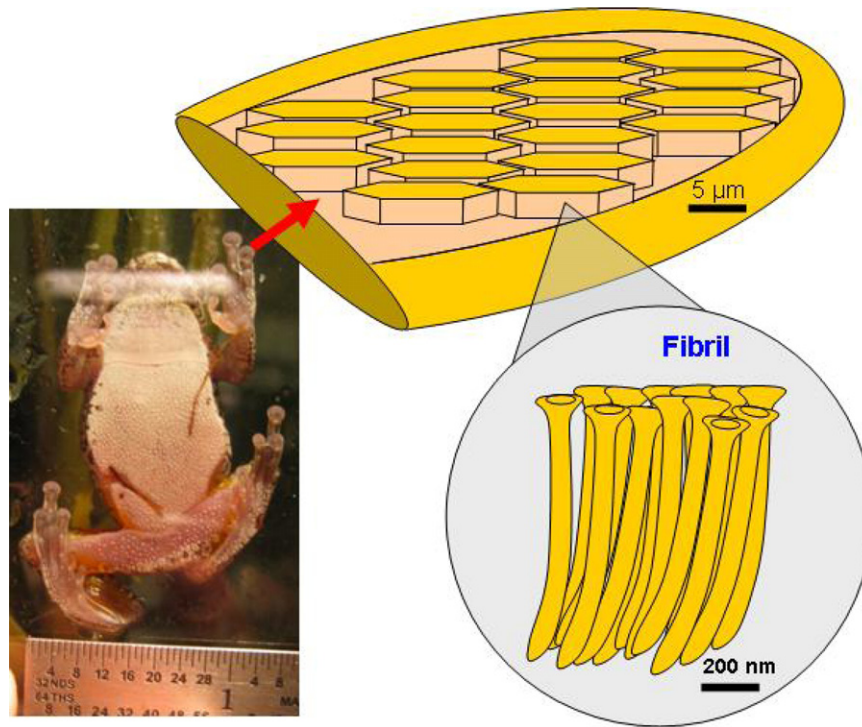


Fig. 30 – Schematic diagram of the structural hierarchy found in the toe pad of a Brazilian tree frog (*Scynax perereca*).

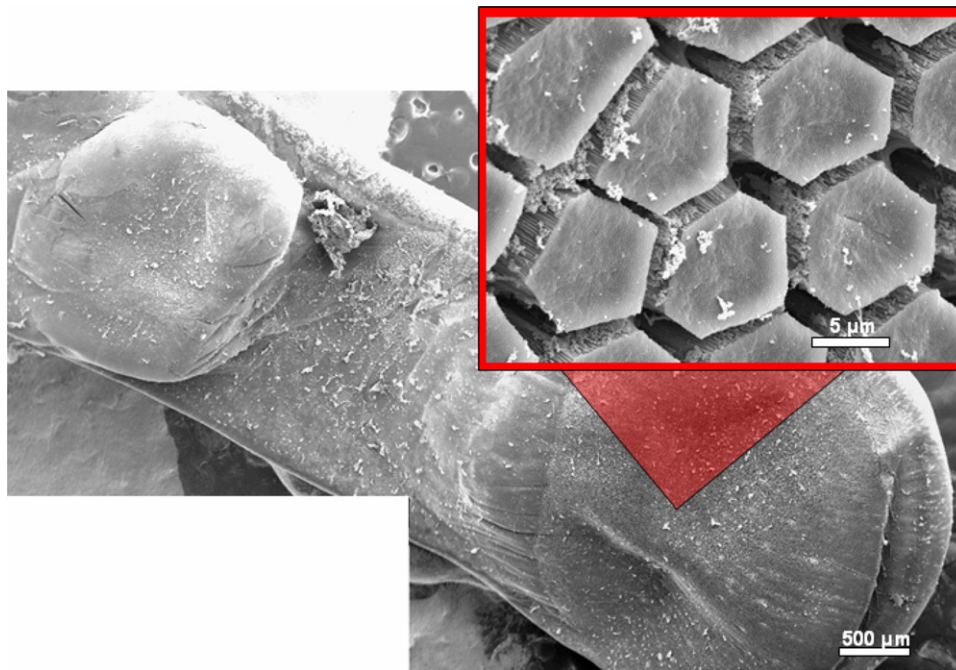


Fig. 31 – Scanning electron micrograph of the toe pad of a Brazilian tree frog; (a) low magnification view of single toe, (b) hexagonal subsections found on the contact surface of the toe pad.

P_0 , is equal to P_{atm} when no external detachment force is applied. As F_d increases, P_0 decreases. Once it becomes zero, detachment occurs. Fig. 39(c) shows the situation for a non-conforming material: A continuous fluid path for the interface region ensures pressure equilibration around the animal and

effectively eliminates suction. It is proposed that capillarity and van der Waals forces can maintain the intimate contact between the ventral side of the foot pedal and the attachment surface; in this manner the suction force can reach and even exceed P_{atm} .

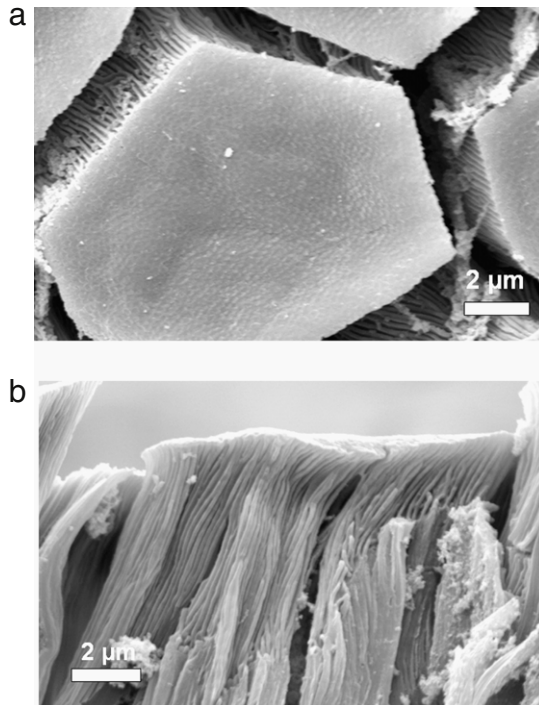


Fig. 32 – Scanning electron micrographs of hexagonal subdivisions: (a) top-down view; (b) side view.

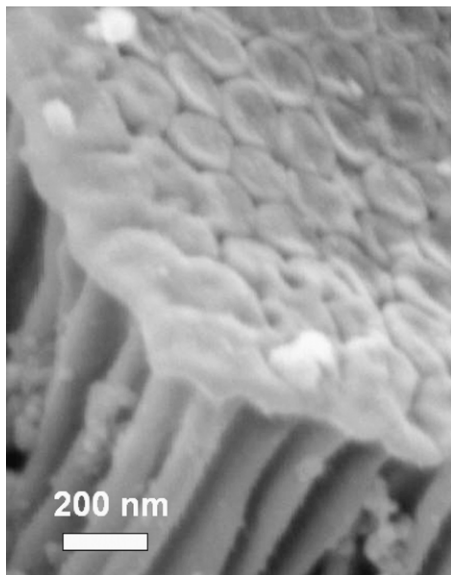


Fig. 33 – High magnification of individual fibers comprising the larger hexagonal subdivisions.

5. Bioinspired materials and structures

This is the most difficult of the three areas delineated in Section 1, both experimentally and analytically. The study of biological materials is benefitting from the modern analytical, characterization, and computational tools and by the ever increasing numbers of investigators combing the field, globally. Bio and biomedical materials are in synergy with advances made in materials synthesis and processing,

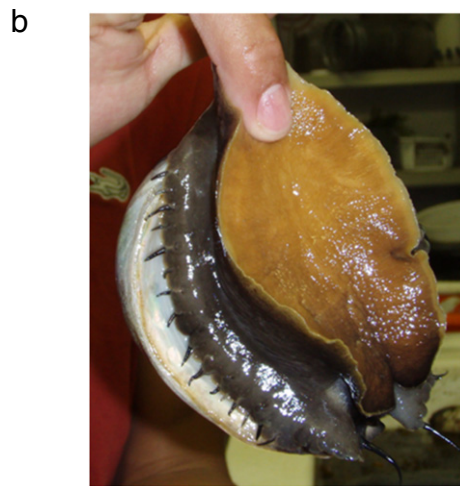


Fig. 34 – The pedal foot of the red abalone: (a) optical image of bottom surface of foot; (b) abalone supporting its own hanging weight through single contact point. Source: Adapted from Lin et al., *Acta Mater.* (2009).

and with the ever better understanding of material–organism interaction. But the third, bioinspired design, poses the greatest challenge. The development and implementation of concepts learned from nature can exist at two levels:

- Design, using concepts from nature but applying synthetic materials and conventional processing methods.
- Molecular-based bioinspired structures. In this approach, we mimic nature all the way down to the molecular level, using biological approach of self-assembly and molecular engineering.

The first approach is much more conventional and has been implemented successfully in a number of applications. We will focus on only a few to illustrate this concept. From the historical and commercial success viewpoint, the discovery by George de Mistral of burrs that stuck stubbornly to his pants and hunting dog is illustrative of the approach. Fig. 40(a) shows the tip of a curved burr found in European countryside. These tips have characteristic hooks which render them particularly attachable to fur in animals and, more recently, loops in clothing. The plants use this strategy to spread the seeds around. This principle was used by George de Mistral

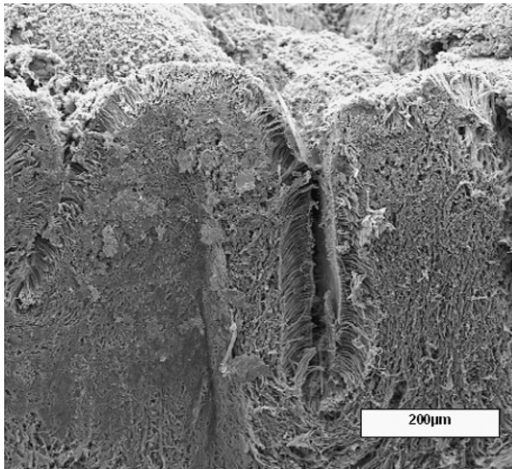


Fig. 35 – Scanning electron microscopy of foot tissue cross-section, the top of the image represents the contact surface of the foot.

Source: Adapted from [Lin et al., Acta Mater. \(2009\)](#).

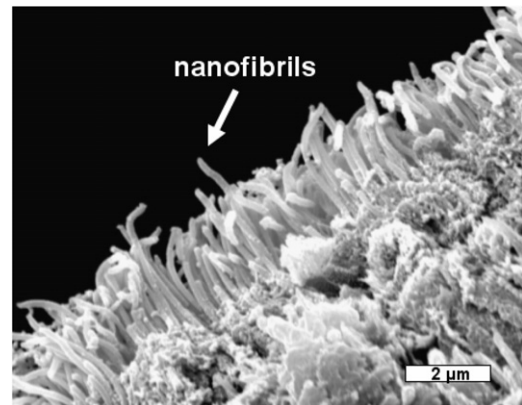


Fig. 37 – Nanofibrils uniaxially aligned along the outer surface of the foot tissue.

Source: Adapted from [Lin et al., Acta Mater. \(2009\)](#).

in the development of VELCRO (from VELours CROchet). [Fig. 40\(b\)](#) shows synthetic hooks embedded in the fabric. They were initially loops with $\sim 200 \mu\text{m}$ diameter, on the same order

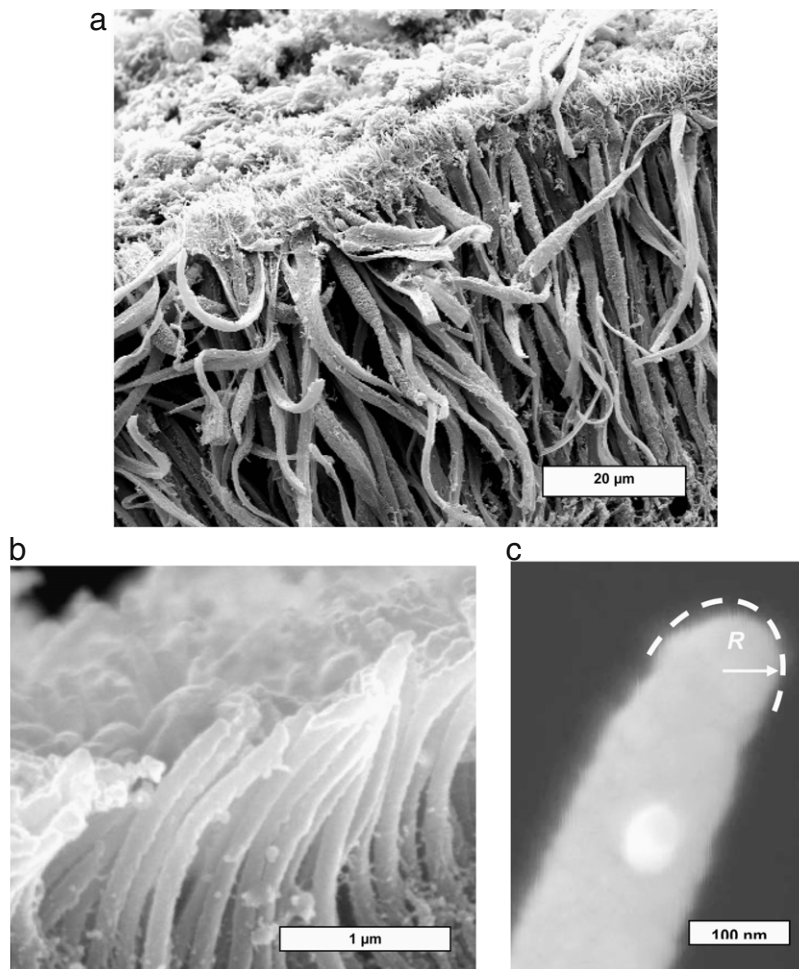


Fig. 36 – SEM characterization of abalone foot tissue: (a) seta lining the outer surface of the foot; (b) nanofibers uniaxially aligned on seta; (c) single nanofiber with hemispherical tip.

Source: Adapted from [Lin et al., Acta Mater. \(2009\)](#).

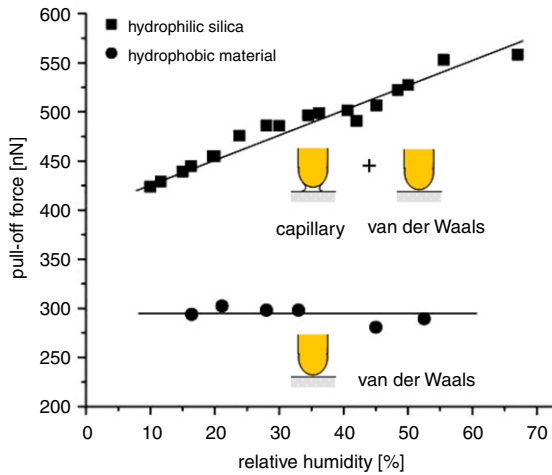


Fig. 38 – Pull-off force as a function of relative humidity of a single seta on a hydrophobic and a hydrophilic substrate. Source: Adapted from Lin et al., Acta Mater. (2009).

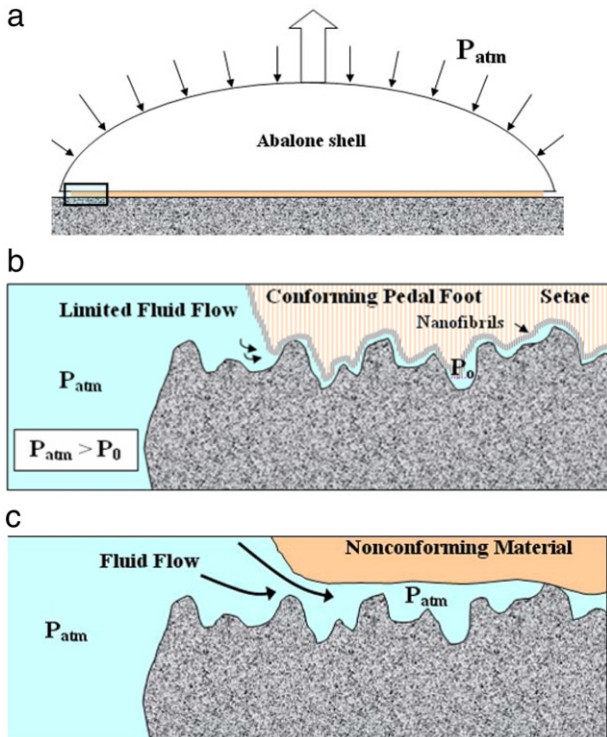


Fig. 39 – Schematic representation of how suction might generate attachment forces. Source: Adapted from Lin et al., Acta Mater. (2009).

as burrs, which are severed, separating the regions A and B in Fig. 40(b), which were initially connected. The loop portion of Velcro is shown in Fig. 40(c). It is an irregular array of fibers with $\sim 50 \mu\text{m}$ thickness.

Another application that is generating considerable excitement is the use of the hydrophobicity of the lotus flower for self-cleaning surfaces. This effect was studied by Barthlott and Ehler (1977), Barthlott (1990), Barthlott and Neinhuis (1997) and recently reviewed by Koch et al. (2009). Fig. 41(a)

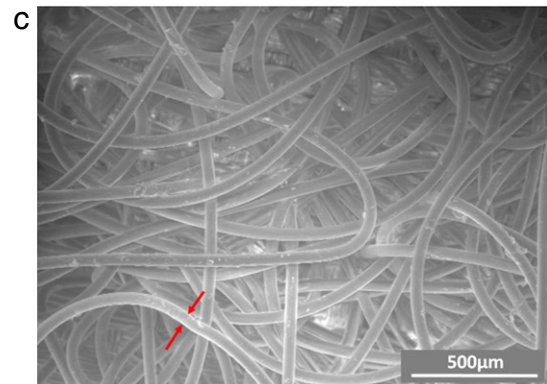
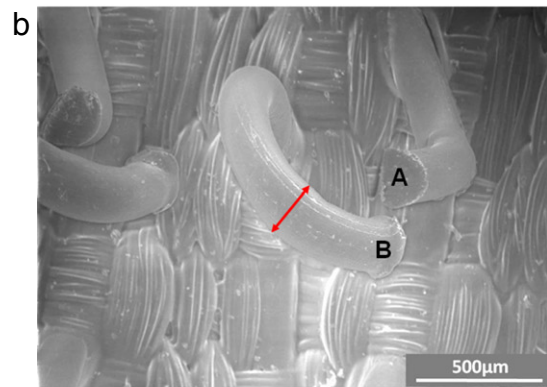
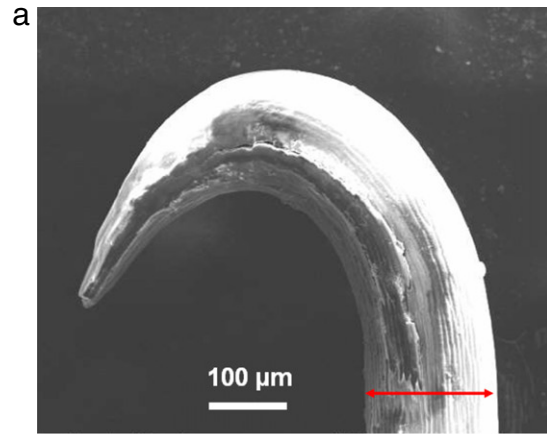


Fig. 40 – SEM micrographs showing the microstructure of (a) a seed-bearing burr; (b,c) hooks and loops in Velcro.

shows a lotus leaf floating on water. The water at its top does not wet it, but concentrates into small areas by virtue of the hydrophobicity of the surface. This is necessary to clean the lotus leaf and ensure its flotation. Drops of water will just roll off the leaf (shown in the right photograph of figure).

The surface of the lotus leaf has small pillars of a few micrometers height and spaced $\sim 20 \mu\text{m}$ (Fig. 41(b)). These are, in turn, covered by smaller scale protrusions, with dimensions of $\sim 0.2\text{--}1 \mu\text{m}$. These are, in their turn, covered with wax. The net result is that the angle of contact between water droplets and the surface is dramatically increased. Hydrophilic surfaces have contact angles below 90° , whereas hydrophobic surfaces have angles above 90° .

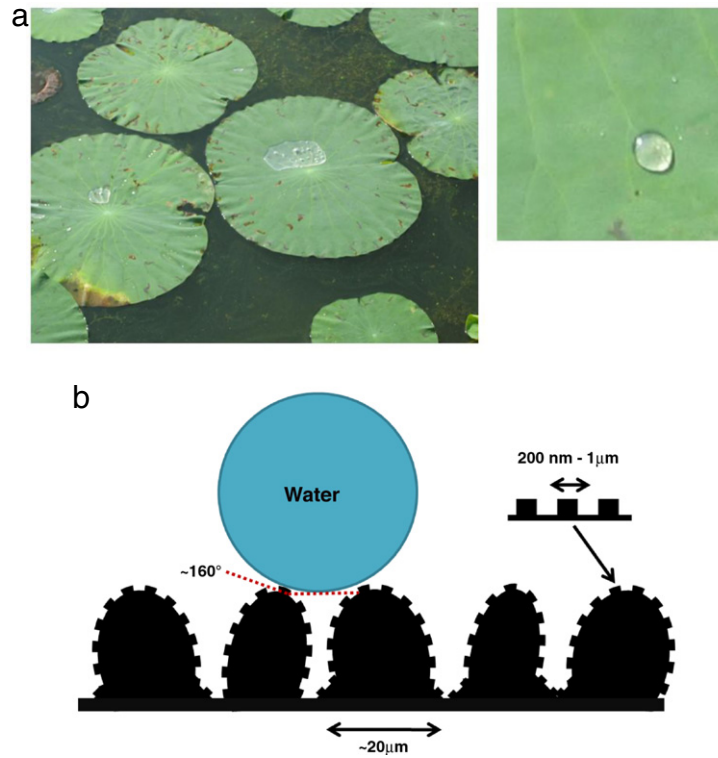


Fig. 41 – The lotus leaf effect: (a) lotus leaf upon which water does not wet; (b) schematic of the surface showing two scales of protrusions which lead to an angle greater than 90° .

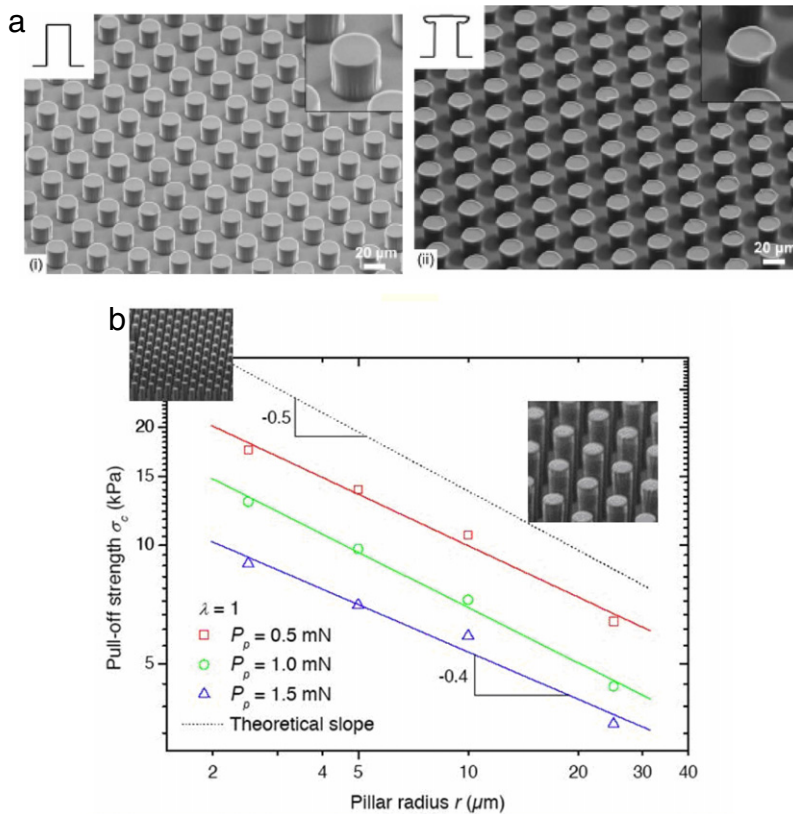


Fig. 42 – (a) SEM micrographs showing micro-pillar arrays with cylindrical and mushroom-like geometries; (b) Pull-off strength increases with decreasing pillar radius.

Source: Adapted from Del Campo et al. (2007b), Greiner et al. (2007).

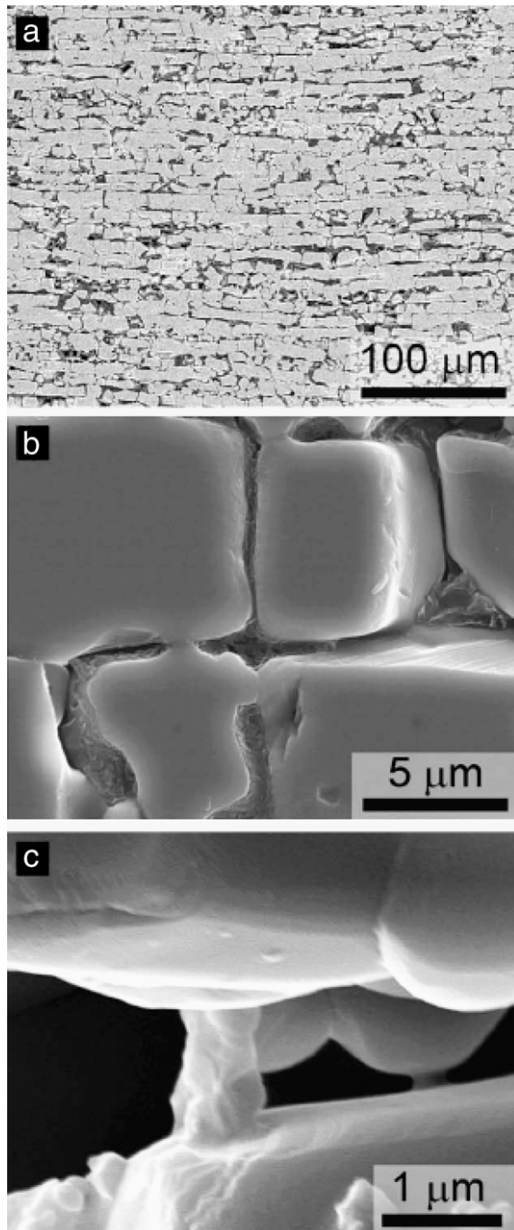


Fig. 43 – Microstructure of abalone nacre-inspired $\text{Al}_2\text{O}_3/\text{PMMA}$ composites in (a) lamellar and (b) brick-and-mortar forms produced by freeze casting techniques; (c) bridge between two tile layers. Source: Launey et al., *Acta Mater.* (2009).

For the lotus, this angle can be as high as 160° , and it is therefore called super-hydrophobic. This hydrophobicity has an important effect: water droplets, almost perfect spheres, can roll over the surface. When they do this, they pick up dust particles which decrease their surface energy by being absorbed into the water droplets. Thus, the surface cleans itself. In 1999, a commercial and very successful product was launched: the facade paint *Lotusan* has been applied on more than 500,000 buildings worldwide so far. Other applications are self-cleaning glasses installed in the sensors of traffic control units on German highways and coatings applied to

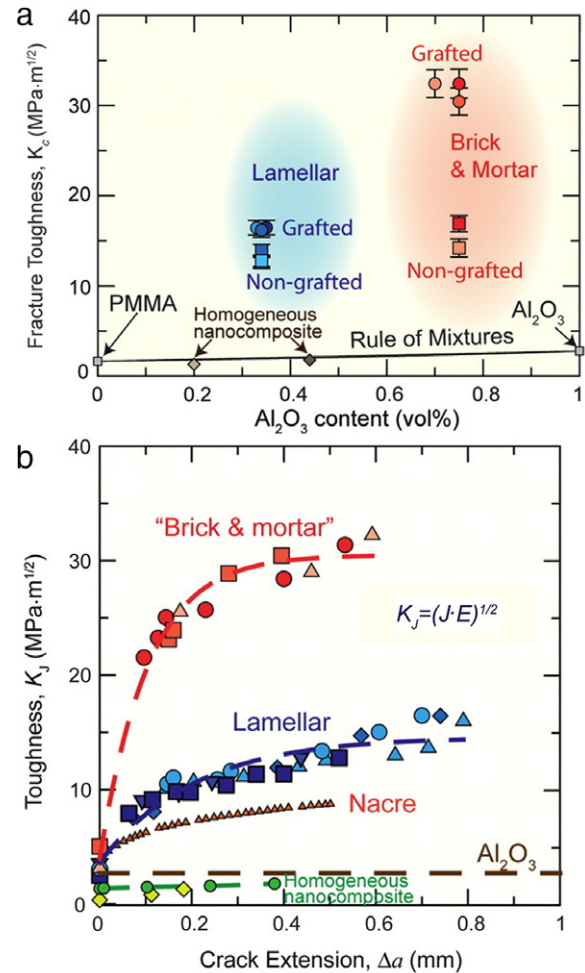


Fig. 44 – (a) Fracture toughness for lamellar and brick-and-mortar composites compared with that for Al_2O_3 and PMMA. Both types of composites are significantly tougher than their constituents. (b) The composites show significant rising R-curve behavior due to micro- and nanoscale toughening mechanisms. Source: Adapted from Munch et al., *Science* (2008).

microwave antennae which help to keep them dust free and decrease the buildup of ice and snow.

The gecko attachment principle has given rise to extensive research in the hope of creating structures that have reversible attachment properties. We illustrate here one successful program that has generated surfaces with pillars that have demonstrated excellent attachment capability. Arzt et al. (2003), Huber et al. (2005), Del Campo et al. (2007a,b), Greiner et al. (2007) and Greiner et al. (2009) have made significant progress in mimicking the structure of the gecko foot by using polydimethylsiloxane (PDMS) surfaces, patterned with fibrils having different termination shapes. Shown in Fig. 42(a) are flat and mushroom shapes. The mushroom shape had a pull-off force approximately 20 times that for surfaces patterned with fibrils having simple semi-spherical cap geometry.

For flat and mushroom-shaped fibrils, exceptionally high adhesion strength values, approaching and exceeding that of

the natural attachment of the gecko, were found. The sizes of the pillars were also changed and it was found that the pull-off force of flat pillars increased with the decrease in radius, i.e., the force is proportional to $R^{-1/2}$. These results are shown in Fig. 42(b). The size dependence of Eq. (13) applies to semi-spherical caps where the JKR equation can be applied directly. Assuming geometrical similarity, the pull off stress should be proportional to $1/R$. In the case of a flat punch, the JKR equation does not apply and σ is proportional to $R^{-1/2}$ (Chan et al., 2007).

The recent development of a gecko-inspired tissue adhesive for biomedical applications by Langer, Karp, and co-workers (Mahdavi et al., 2008) also has great potential. They demonstrated that gecko-inspired arrays of pillars of PGSA (polyglycerol sebacate acrylate) provided attachment under water. This tape is proposed as a biodegradable polymer adhesive to tissue. The adhesion was tested *in vitro* to porcine intestine and *in vivo* to rat abdominal muscle. Carbon nanotube arrays are also being proposed to form fibrillar arrays and have self-cleaning properties due to extreme hydrophobicity (Sethi et al., 2008). The effects of angled fibrillar attachments have also been investigated and it was demonstrated to have an important bearing.

At UC Berkeley and Lawrence Berkeley National Lab, a research group led by Ritchie and Tomsia (Deville et al., 2006a,b; Munch et al., 2008; Launey et al., 2009, 2010b) mimicked the abalone's toughening mechanisms by combining aluminum oxide and polymethyl methacrylate (PMMA). They used an ice-templated manufacturing technique to create the lamellar structure in alumina and were able to achieve outstanding mechanical properties. The structure has several of the basic components of nacre as can be seen by comparing Fig. 43(a) with Fig. 16(b) and 17. The tiles are present (alumina instead of aragonite) with the organic interlayer being replaced by PMMA. It should be noticed that their thickness is considerably higher than in nacre, $\sim 10 \mu\text{m}$ versus $\sim 0.5 \mu\text{m}$. There are bridges between the tiles, shown in Fig. 16(b) and 43(b). The final product is a solid ceramic-based laminate composite with a high yield strength and fracture toughness. For a 80% Al_2O_3 -20% PMMA laminate, a tensile strength of 200 MPa and fracture toughness of $30 \text{ MPa}\cdot\text{m}^{1/2}$ are obtained. These values represent specific properties comparable to those of aluminum alloys. It should be noted that this is accomplished with the majority being alumina. The resistance to crack propagation (R curve behavior) is shown in Fig. 44(b). The increase in toughness with crack propagation is obvious. The curve rises to $K_{\text{IC}} = 30 \text{ MPa}\cdot\text{m}^{1/2}$. This is in stark contrast with monolithic alumina, which has a flat curve with $K_{\text{IC}} = 1 \text{ MPa}\cdot\text{m}^{1/2}$. One unique aspect of the architecture of this bioinspired material is that when it has the abalone brick-and-mortar structure with bridges between the tiles, the toughness is increased over the purely lamellar structure ($\sim 15 \text{ MPa}\cdot\text{m}^{1/2}$). The more conventional simple laminate structure is definitely less tough than the new material. This example illustrates the potential of (a) understanding and (b) mimicking biological materials.

6. Conclusions

Given below are some broad conclusions which show the principal attributes of the emerging field of biological and bioinspired materials in MSE.

- We are trying to understand the structure-property relations in biological materials, all the way from the nano to the structural level.
- The connections between the different structural levels and the assembly processes used by organisms to develop their structures are being investigated using the powerful analytical, experimental, and computational arsenal of MSE.
- We illustrated a number of essential concepts with, primarily, the results of our research. Thus, this overview is limited in scope and only captures a small fraction of the work being carried out.
- Recognizing the limited supply of materials available in biological systems and the narrow range of temperatures in which synthesis and processing takes place, we should use the design principles of nature to amplify their effectiveness. Our current technological capabilities can expand the biological manufacturing principles to a broader range of temperatures, pressures, and compositions, while retaining the essential features.
- Biomimicking is evolving from purely synthetic processes using design concepts from nature (such as, for instance, VELCRO) to molecular-based processing in which self-assembly and other unique natural processes of nature are used.
- We foresee continued and expanded activity in the field of biological and bioinspired materials as large numbers of investigators globally explore natural materials and discover new structural designs and concepts. This expansion in our understanding will be (and already is) paralleled by a whole array of novel synthesis and processing methods to produce bioinspired materials and structures. Aizenberg's (2010) recent MRS lecture is a stellar example of this effort.

Acknowledgements

This research was supported by The National Science Foundation Division of Materials Research, Biomaterials Program, Grant DMR 0510138. We thank Profs. J. McKittrick, C.T. Lim, and R.O. Ritchie for helpful discussions. We also thank Eddie Kisfaludi for taking care of the abalone, S.G. Bodde for providing figures, and Ryan Anderson (CALIT2) and C.T. Wei for the use of the SEM. We thank the referees for their thoughtful comments which enriched this manuscript. In particular, the fourth paragraph in the Introduction is taken from the comments by one of them.

REFERENCES

- Aizenberg, J., 2010. New nanofabrication strategies: inspired by mineralization. *MRS Bull.* 35, 323–330.
- Arzt, E., 2006. Biological and artificial attachment devices: Lessons for materials scientists from flies and geckos. *Mater. Sci. Eng. C* 26, 1245–1250.
- Arzt, E., Gorb, S., Spolenak, R., 2003. Evidence for van der Waals adhesion in gecko setae. *Proc. Natl. Acad. Sci. USA* 100, 10603–10606.
- Autumn, K., Sitti, M., Liang, Y.A., Peattie, A.M., Hansen, W.R., Sponberg, S., Kenny, T.W., Fearing, R., Israelachvili, J.N., Full, R.J., 2002. Evidence for van der Waals adhesion in gecko setae. *Proc. Natl. Acad. Sci. USA* 99, 12252–12256.
- Barnes, W.J.P., 2007. Functional morphology and design constraints of smooth adhesive pads. *MRS Bull.* 32, 479–485.
- Barnes, W.J.P., Perez-Goodwyn, P., Gorb, S.N., 2005. Mechanical properties of the toe pads of the tree frog, *Litoria caerulea*. *Comp. Biochem. Physiol. A* 141, S145.
- Barnes, W.J.P., Oines, C., Smith, J.M., 2006. Whole animal measurements of shear and adhesive forces in adult tree frogs: insights into underlying mechanisms of adhesion obtained from studying the effects of size and shape. *J. Comp. Physiol. A* 192, 1179–1191.
- Barthlott, W., 1990. Scanning electron microscopy of the epidermal surface in plants. In: Claugher, D. (Ed.), *Application of the Scanning EM in Taxonomy and Functional Morphology, Systematics Association's Special Volume*. Clarendon Press, Oxford, pp. 69–94.
- Barthlott, W., Ehler, N., 1977. Raster-Elektronenmikroskopie der Epidermis-Oberflächen von Spermatophyten. *Tropische und subtropische Pflanzenwelt (Akad. Wiss. Lit. Mainz)* 19, 110.
- Barthlott, W., Neinhuis, C., 1997. The purity of sacred lotus or escape from contamination in biological surfaces. *Planta* 202, 1–8.
- Belcher, A.M., Wu, X.H., Christensen, R.J., Hansma, P.K., Stucky, G.D., Morse, D.E., 1996. Control of crystal phase switching and orientation by soluble mollusc-shell proteins. *Nature* 381, 56–58.
- Bell, E.C., Gasoline, J.M., 1996. Mechanical design of mussel byssus: material yield enhances attachment strength. *J. Exp. Biol.* 199, 1005–1017.
- Berglin, M., Gatenholm, P., 2003. The barnacle adhesive plaque: morphological and chemical differences as a response to substrate properties. *Colloids Surf.* 28, 107–117.
- Borah, B., Gross, G., Dufresne, T., Smith, T., Cookman, M., Chmielewski, P., Lundy, M., Hartke, J., Sod, E., 2001. Three-dimensional microimaging (MR μ l and μ CT), finite element modeling, and rapid prototyping provide unique insights into bone architecture in osteoporosis. *Anatom. Rec.* 264, 101–110.
- Buehler, M.J., 2007. Nano- and micromechanical properties of hierarchical biological materials and tissues. *J. Mater. Sci.* 8765–8770.
- Buehler, M.J., Keten, S., Ackbarow, T., 2008. Theoretical and computational hierarchical nanomechanics of protein materials: Deformation and fracture. *Prog. Mater. Sci.* 53, 1101–1241.
- Chan, E.P., Greiner, C., Arzt, E., Crosby, A.J., 2007. Designing model systems for enhanced adhesion. *MRS Bull.* 32, 496–503.
- Checa, A.G., Cartwright, J.H.E., Willinger, M.G., 2009. The key role of the surface membrane in why gastropod nacre grows in towers. *Proc. Natl. Acad. Sci. USA* 106, 38–43.
- Chen, P.-Y., Lin, A.Y.M., Lin, Y.S., Seki, Y., Stokes, A.G., Peyras, J., Olevsky, E.A., Meyers, M.A., McKittrick, J., 2008a. Structure and mechanical properties of selected biological materials. *J. Mech. Behav. Biomed. Mater.* 1, 208–226.
- Chen, P.-Y., Lin, A.Y.M., Lin, Y.S., Seki, Y., Bodde, S.G., Stokes, A.G., McKittrick, J., Meyers, M.A., 2008b. Structural biological materials: overview of current research. *JOM* 60, 23–32.
- Chen, P.-Y., Lin, A.Y.M., McKittrick, J., Meyers, M.A., 2008c. Structure and mechanical properties of crab exoskeletons. *Acta Biomater.* 4, 587–596.
- Chen, P.-Y., Stokes, A.G., McKittrick, J., 2009. Comparison of structure and mechanical properties of bovine femur bone and antlers of the North American elk (*Cervus canadensis*). *Acta Biomater.* 5, 693–706.
- Del Campo, A., Greiner, C., Alvarez, I., Arzt, E., 2007a. Patterned Surfaces with Pillars with 3D Tip Geometry Mimicking Bioattachment Devices. *Adv. Mater.* 19, 1973–1977.
- Del Campo, A., Greiner, C., Alvarez, I., Arzt, E., 2007b. Contact shape controls adhesion of bioinspired fibrillar surfaces. *Langmuir* 23, 10235–10243.
- Deville, S., Saiz, E., Nalla, R.K., Tomsia, A.P., 2006a. Freezing as a path to build complex composites. *Science* 311, 515–518.
- Deville, S., Saiz, E., Tomsia, A.P., 2006b. Freeze casting of hydroxyapatite scaffolds for bone tissue engineering. *Biomaterials* 27, 5480–5489.
- Donovan, D.A., Carefoot, T.H., 1997. Locomotion in the abalone *Haliotis kamtschatkana*: pedal morphology and cost of transport. *J. Exp. Biol.* 200, 1145–1153.
- Ehrlich, H., 2010. Chitin and collagen as universal and alternative templates in biomineralization. *Int'l. Geology Rev.* 52, 661–699.
- Ernst, V.V., 1973a. The digital pads of the tree frog *Hyla cinerea*. I. The epidermis. *Tissue Cell* 5, 83–96.
- Ernst, V.V., 1973b. The digital pads of the tree frog *Hyla cinerea*. II. The mucous glands. The epidermis. *Tissue Cell* 5, 97–104.
- Espinosa, H.D., Rim, J.E., Barthelat, F., Buehler, M.J., 2009. Merger of structure and material in nacre and bone — Perspectives on de novo biomimetic materials. *Prog. Mater. Sci.* 54, 1059–1100.
- Fratzl, P., Weinkamer, R., 2007. Nature's hierarchical materials. *Prog. Mater. Sci.* 52, 1263.
- Fratzl, P. (Ed.), 2008. *Collagen: Structure and Mechanics*. Springer, New York.
- Fritz, M., Belcher, A.M., Radmacher, M., Walters, D.A., Hansma, P.K., Strucky, G.D., Morse, D.E., Mann, S., 1994. Flat pearls from biofabrication of organized composites on inorganic substrates. *Nature* 371, 49.
- Fung, Y.C., 1993. *Biomechanics: Mechanical Properties of Living Tissues*, 2nd edition. Springer-Verlag, New York.
- Gao, H., Ji, B., Jäger, I.L., Arzt, E., Fratzl, P., 2003. Materials become insensitive to flaws at nanoscale: lessons from nature. *Proc. Natl. Acad. Sci. USA* 100, 5597–5600.
- Gao, H., 2006. Application of fracture mechanics concepts to hierarchical biomechanics of bone and bone-like materials. *Int'l. J. Fracture.* 138, 101–137.
- Gibson, L.J., Ashby, M.F., 1997. *Cellular Solids: Structure and Properties*, 2nd edition. Cambridge University Press, Cambridge.
- Green, D.M., 1979. Tree frog toe pads: comparative surface morphology using scanning electron microscopy. *Can. J. Zool.* 57, 2033–2046.
- Green, D.M., Simon, P., 1986. Digital microstructure in ecologically diverse sympatric microhylid frogs, genera *Cophixalus* and *Sphenophryne* (Amphibia: Anura). Papua New Guinea. *Aust. J. Zool.* 34, 135–145.
- Greiner, C., Arzt, E., Del Campo, A., 2009. Hierarchical gecko-like adhesives. *Adv. Mater.* 21, 479–482.
- Greiner, C., Del Campo, A., Arzt, E., 2007. Adhesion of bioinspired micro-patterned surfaces: effects of pillar radius, aspect ratio, and preload. *Langmuir* 23, 3495–3502.
- Hanna, G., Barnes, W.J.P., 1991. Adhesion and detachment of the toe pads of treefrogs. *J. Exp. Biol.* 155, 103–125.

- Huber, G., Mantz, H., Spolenak, R., Mecke, K., Jacobs, K., Gorb, S.N., Arzt, E., 2005. Proc. Natl. Acad. Sci. USA 102, 16293–16296.
- Jäger, I., Fratzl, P., 2000. Mineralized collagen fibrils: a mechanical model with a staggered arrangement of mineral particles. Biophys. J. 79, 1737–1746.
- Ji, B., Gao, H., 2004. Mechanical properties of nanostructure of biological materials. J. Mech. Phys. Solids 52, 1963–1990.
- Johnson, K.L., Kendall, K., Roberts, A.D., 1971. Surface energy and the contact of elastic solids. Proc. Roy. Soc. London 324, 301–313.
- Kamat, S., Su, X., Ballarini, R., Heuer, A.H., 2000. Structure basis for the fracture toughness of the shell of the conch *Strombus gigas*. Nature 405, 1036–1040.
- Kamat, S., Kessler, H., Su, X., Ballarini, R., Nassirou, M., Heuer, A.H., 2004. Fracture mechanisms of the *Strombus gigas* conch shell: II-micromechanics analyses of multiple cracking and large-scale crack bridging. Acta Mater. 52, 2395–2406.
- Karam, G.N., Gibson, L.J., 1995. Elastic buckling of cylindrical shells with elastic cores-I: analysis. Int. J. Solids Struct. 32, 1259–1283.
- Koch, K., Bhushan, B., Barthlott, W., 2009. Multifunctional surface structures of plants: An inspiration for biomimetics. Prog. Mater. Sci. 54, 137–178.
- Launey, M.E., Munch, E., Alsem, D.H., Barth, H.D., Saiz, E., Tomsia, A.P., Ritchie, R.O., 2009. Designing highly toughened hybrid composites through nature-inspired hierarchical complexity. Acta Mater. 57, 2919–2932.
- Launey, M.E., Chen, P.-Y., McKittrick, J., Ritchie, R.O., 2010a. Mechanistic aspects of the fracture toughness of elk antler bone. Acta Biomater. 6, 1505–1514.
- Launey, M.E., Munch, E., Alsem, D.H., Saiz, E., Tomsia, A.P., Ritchie, R.O., 2010b. A novel biomimetic approach to the design of high-performance ceramic/metal composites. J. R. Soc. Inter. 7, 741–753.
- Lin, A.Y.M., Structural and functional biological materials: abalone nacre, sharp materials, and abalone foot adhesion, Doctoral Dissertation, U. C. San Diego, 2008.
- Lin, A.Y.M., Meyers, M.A., 2005. Growth and structure in abalone shell. Mater. Sci. Eng. A 290, 27–41.
- Lin, A.Y.M., Chen, P.-Y., Meyers, M.A., 2008. The growth of nacre in the abalone shell. Acta Biomater. 4, 131–138.
- Lin, A.Y.M., Meyers, M.A., 2009. The interfacial shear strength in abalone nacre. J. Mech. Behav. Biomed. Mater. 2, 607–612.
- Lin, A.Y.M., Brunner, R., Chen, P.-Y., Talke, F.E., Meyers, M.A., 2009. Underwater adhesion of abalone: The role of van der Waals and capillary forces. Acta Mater. 57, 4178–4185.
- Lopez, M.I., Chen, P.-Y., McKittrick, J., Meyers, M.A., 2010. Growth of nacre in abalone: Seasonal and feeding effect. Mater. Sci. Eng. C, in press (doi:10.1016/j.msec.2010.09.003).
- Lowenstam, H.A., Weiner, S., 1989. On Biomineralization. Oxford University Press, New York.
- Mahdavi, A., Ferreira, L., Sundback, C., Nichol, J., Chan, E., Carter, D., Bettinger, C., Patavanich, S., Chignozha, L., Joseph, E., Galakatos, A., Pryor, A., Pomerantseva, I., Masiakos, P., Faquin, W., Zumbuehl, A., Hong, S., Borenstein, J., Vacanti, J., Langer, R., Karp, J., 2008. A biodegradable and biocompatible gecko-inspired adhesive. Proc. Natl. Acad. Sci. USA 105, 2307–2312.
- Mann, S., 2001. Biomineralization: Principles and Concepts in Bioinorganic Materials Chemistry. Oxford University Press, New York.
- Mann, S., Archibald, D.D., Didymus, J.M., Douglas, T., Heywood, B.R., Meldrum, F.C., Reeves, N.J., 1993. Crystallization and inorganic-organic interfaces — biominerals and biomimetic synthesis. Science 261, 1286–1292.
- Mayer, G., 2005. Rigid biological systems as models for synthetic composites. Science 310, 1144–1147.
- McAllister, A., Channing, L., 1983. Comparisons of toe pads of some Southern African climbing frogs. S. Afr. J. Zool. 18, 110–114.
- McKittrick, J., Chen, P.-Y., Tombolato, L., Novitskaya, E.E., Trim, W., Lin, Y.S., Hirata, G.A., Olevsky, E.A., Horstemeyer, M.F., Meyers, M.A., 2010. Energy absorbent natural materials and bio-inspired design strategies: A review. Mater. Sci. Eng. C 30, 331–342.
- Meyers, M.A., Lin, A.Y.M., Seki, Y., Chen, P.-Y., Kad, B., Bodde, S.G., 2006. Structural biological composites: an overview. JOM 58, 35–41.
- Meyers, M.A., Chen, P.-Y., Lin, A.Y.M., Seki, Y., 2008a. Biological materials: structure and mechanical properties. Prog. Mater. Sci. 53, 1–206.
- Meyers, M.A., Lin, A.Y.M., Chen, P.-Y., Mueyco, J., 2008b. Mechanical strength of abalone nacre: role of the soft organic layer. J. Mech. Behav. Biomed. Mater. 1, 76–85.
- Meyers, M.A., Lim, C.T., Li, A., Hairul Nizam, B.R., Tan, E.P.S., Seki, Y., McKittrick, J., 2009. The role of organic intertile layer in abalone nacre. Mater. Sci. Eng. C 29, 2398–2410.
- Meyers, M.A., Lin, Y.S., Olevsky, E.A., Chen, P.-Y., 2010. Battle in the Amazon: Arapaima (Pirarucu) vs. Serrasalminae (Piranha) (in preparation).
- Müller, R., Rügsegger, P., 1995. Three-dimensional finite element modelling of non-invasively assessed trabecular bone structures. Med. Eng. Phys. 17, 126–133.
- Munch, E., Launey, M.E., Alsem, D.H., Saiz, E., Tomsia, A.P., Ritchie, R.O., 2008. Tough bio-inspired hybrid materials. Science 322, 1515–1520.
- Nagaraja, S., Couse, T.L., Guldberg, R.E., 2004. Trabecular bone microdamage and microstructural stresses under uniaxial compression. J. Biomech. 38, 707–716.
- Nalla, R.K., Kinney, J.H., Ritchie, R.O., 2003. Mechanistic fracture criteria for the failure of human cortical bone. Nature Mater. 2, 164.
- Nalla, R.K., Kruzic, J.J., Kinney, J.H., Ritchie, R.O., 2005. Mechanistic aspects of fracture and R-curve behavior in human cortical bone. Biomaterials 26, 217.
- Rho, J.Y., Kuhn-Spearing, L., Zioupos, P., 1998. Mechanical properties and the hierarchical structure of bone. Med. Eng. Phys. 20, 92.
- Rietbergen, B.V., Weinans, H., Huiskes, R., Odgaard, A., 1995. A new method to determine trabecular bone elastic properties and loading using micromechanical finite element models. J. Biomech. 12, 69–81.
- Sarikaya, M., Gunnison, K.E., Yasrebi, M., Aksay, J.A., 1990. Mechanical property-microstructural relationships in abalone shell. Mater. Res. Soc. 174, 109–116.
- Saunders, M., Kong, C., Shaw, J.A., Macey, D.J., Clode, P.L., 2009. Characterization of biominerals in the radula teeth of the chiton, *Acanthopleura hirtosa*. J. Struct. Biol. 167, 55–61.
- Seki, Y., Schneider, M.S., Meyers, M.A., 2005. Structure and mechanical properties of the toucan beak. Acta Mater. 53, 5281–5296.
- Seki, Y., Kad, B., Benson, D., Meyers, M.A., 2006. The toucan beak: Structure and mechanical response. Mater. Sci. Eng. C 26, 1412–1420.
- Seki, Y., Bodde, S.G., Meyers, M.A., 2010. Toucan and hornbill beaks: a comparative study. Acta Biomater. 6, 331–343.
- Sethi, S., Ge, L., Ajayan, P.M., Dhinojwala, A., 2008. Gecko-inspired carbon nanotube based self cleaning adhesives. Nano Lett. 8, 822–825.
- Shen, X., Belcher, A.M., Hansma, P.K., Stucky, G.D., Morse, D.E., 1997. Molecular cloning and characterization of Lustrin A, a matrix protein from shell and pearl nacre of *Haliotis rufescens*. J. Biol. Chem. 272, 32472–32481.
- Song, F., Zhang, X.H., Bai, Y.L., 2002. Microstructure and characteristics in the organic matrix layers of nacre. J. Mater. Res. 17, 1567–1570.

- Song, F., Soh, A.K., Bai, Y.L., 2003. Structural and mechanical properties of the organic matrix layers of nacre. *Biomaterials* 24, 3623.
- Stella, J.A., D'Amore, A., Wagner, W.R., Sacks, M.S., 2010. On the biomechanical function of scaffolds for engineering load-bearing soft tissues. *Acta Biomater.* 6, 2365–2381.
- Tombolato, L., Novitskaya, E.E., Chen, P.-Y., Sheppard, F.A., McKittrick, J., 2010. Microstructure, elastic and fracture properties of horn keratin. *Acta Biomater.* 6, 319–330.
- Trueman, E.R., Hodgson, A.N., 1990. The fine structure and function of the foot of *Nassarius krausslanus*, a gastropod moving by ciliary locomotion. *J. Moll. Stud.* 56, 221–228.
- Ugural, A.C., Fenster, S.K., 1987. *Advanced Strength and Applied Elasticity*. Prentice Hall, New Jersey.
- Ulrich, D., Rietbergen, B.V., Weinas, H., Regsegger, P., 1998. Finite element analysis of trabecular bone structure: A comparison of image-based meshing techniques. *J. Biomech.* 31, 1187–1192.
- Vincent, J.F.V., Currey, J.D. (Eds.), 1980. *Mechanical Properties of Biological Materials*. Cambridge University Press, Cambridge.
- Vincent, J.F.V., 1991. *Structural Biomaterials*. Princeton University Press, New Jersey.
- Waite, J.H., Tanzer, M.L., 1981. Polyphenolic substance of *Mytilus edulis* — novel adhesive containing L-DOPA and hydroxyproline. *Science* 212, 1038.
- Waite, J.H., 1987. Nature's underwater adhesive specialist. *Int. J. Adhes. Adhes.* 7, 9.
- Weaver, J.C., Wang, Q., Miserez, A., Tantuccio, A., Stromberg, R., Bozhilov, K.N., Maxwell, P., Nay, R., Heier, S.T., DiMasi, E., Kisailus, D., 2010. Analysis of an ultra hard magnetic biomineral in chiton radular teeth. *Mater. Today* 13, 42–52.
- Weiner, S., Addadi, L., 1997. Design strategies in mineralized biological materials. *J. Mater. Chem.* 7, 689–702.
- Weiner, S., Wagner, H.D., 1998. The material bone: structure mechanical function relations. *Annu. Rev. Mater. Sci.* 28, 271.
- Welsh, U., Storch, V., Fuchs, W., 1974. The fine structure of the digital pads of rhacophorid tree frogs. *Cell Tissue Res.* 148, 407–416.
- Yang, Q.D., Cox, B.N., Nalla, R.K., Ritchie, R.O., 2006. Fracture length scales in human cortical bone: The necessity of nonlinear fracture models. *Biomaterials* 27, 2095.
- Yao, H., Gao, H., 2008. Multi-scale cohesive laws in hierarchical materials. *Intl. J. Solids Struct.* 45, 3627–3643.